

The HST Legacy Archival Uniform Reduction of Local Group Imaging (LAURELIN). I. Photometry and Star Formation Histories for 36 Ultra-faint Dwarf Galaxies

MEREDITH J. DURBIN,¹ YUMI CHOI,² ALESSANDRO SAVINO,¹ DANIEL R. WEISZ,¹ ANDREW E. DOLPHIN,^{3,4}
JULIANNE J. DALCANTON,^{5,6} MYOUNGWON JEON,^{7,8} NITYA KALLIVAYALIL,⁹ TING S. LI,¹⁰ ANDREW B. PACE,⁹
EKTA PATEL,^{11,*} ELENA SACCHI,¹² EVAN D. SKILLMAN,¹³ SANGMO TONY SOHN,^{14,8} ROELAND P. VAN DER MAREL,^{14,15}
ANDREW WETZEL,¹⁶ AND BENJAMIN F. WILLIAMS⁶

¹*Department of Astronomy, University of California, Berkeley, Berkeley, CA 94720, USA*

²*NSF National Optical-Infrared Astronomy Research Laboratory, 950 N. Cherry Avenue, Tucson, AZ 85719 USA*

³*Raytheon Technologies, 1151 E. Hermans Road, Tucson, AZ 85756, USA*

⁴*University of Arizona, Steward Observatory, 933 North Cherry Avenue, Tucson, AZ 85721, USA*

⁵*Center for Computational Astrophysics, Flatiron Institute, 162 Fifth Avenue, New York, NY 10010, USA*

⁶*Department of Astronomy, University of Washington, Box 351580, Seattle, WA 98195-1580, USA*

⁷*School of Space Research, Kyung Hee University, 1732 Deogyong-daero, Giheung-gu, Yongin-si, Gyeonggi-do 17104, Republic of Korea*

⁸*Department of Astronomy & Space Science, Kyung Hee University, 1732 Deogyong-daero, Yongin-si, Gyeonggi-do 17104, Republic of Korea*

⁹*Department of Astronomy, University of Virginia, 530 McCormick Road, Charlottesville, VA 22904, USA*

¹⁰*Department of Astronomy and Astrophysics, University of Toronto, 50 St. George Street, Toronto ON, M5S 3H4, Canada*

¹¹*Department of Physics and Astronomy, University of Utah, 115 South 1400 East, Salt Lake City, Utah 84112, USA*

¹²*Leibniz-Institut für Astrophysik Potsdam (AIP), An der Sternwarte 16, 14482 Potsdam, Germany*

¹³*University of Minnesota, Minnesota Institute for Astrophysics, School of Physics and Astronomy, 116 Church Street, S.E., Minneapolis, MN 55455, USA*

¹⁴*Space Telescope Science Institute, 3700 San Martin Drive, Baltimore, MD 21218, USA*

¹⁵*Center for Astrophysical Sciences, The William H. Miller III Department of Physics & Astronomy, Johns Hopkins University, Baltimore, MD 21218, USA*

¹⁶*Department of Physics & Astronomy, University of California, Davis, CA 95616, USA*

ABSTRACT

We present uniformly measured resolved stellar photometry and star formation histories (SFHs) for 36 nearby ($\lesssim 400$ kpc) ultra-faint dwarf galaxies (UFDs; $-7.1 \leq M_V \leq +0.0$) from new and archival *HST* imaging. We measure homogeneous distances to all systems via isochrone fitting and find good agreement ($\leq 2\%$) for the 18 UFDs that have literature RR Lyrae distances. From the ensemble of SFHs, we find: (i) an average quenching time (here defined as the lookback time by which 80% of the stellar mass formed, τ_{80}) of 12.48 ± 0.18 Gyr ago ($z = 4.6_{-0.5}^{+0.6}$), which is compatible with reionization-based quenching scenarios; and (ii) modest evidence of a delay ($\lesssim 800$ Myr) in quenching times of UFDs thought to be satellites of the LMC or on their first infall, relative to long-term Galactic satellites, which is consistent with previous findings. We show that robust SFH measurement via the ancient main sequence turnoff (MSTO) requires a minimum effective luminosity (i.e., luminosity within the observed field of view) of $M_V \leq -2.5$, which corresponds to ~ 100 stars around the MSTO. We also find that increasing the S/N above ~ 100 at the MSTO does not improve SFH precision, which remains dominated by stochastic effects associated with the number of available stars. A main challenge driving the precision of UFD SFHs is limitations in the accuracy of foreground dust maps. We make all photometry catalogs public as the first data release of a larger *HST* archival program targeting all dwarf galaxies within ~ 1.3 Mpc.

Corresponding author: Meredith Durbin

meredith.durbin@berkeley.edu

Keywords: Dwarf galaxies (416) — Galaxy evolution (594) — Galaxy stellar content (621) — Local Group (929) — Reionization (1383) — Star formation (1569)

1. INTRODUCTION

Deep photometric and spectroscopic campaigns over the two last decades have shown that ultra-faint dwarf galaxies (UFDs; $M_V \geq -7.7$, J. D. Simon 2019), the least massive galaxies in the Universe with observable baryons, are extremely metal-poor, ancient, and dark matter dominated systems (e.g., J. T. A. de Jong et al. 2008; J. D. Simon et al. 2010; S. Okamoto et al. 2012; L. C. Vargas et al. 2013; G. Gilmore et al. 2013; T. M. Brown et al. 2014; D. R. Weisz et al. 2014a; A. P. Ji et al. 2019; J. D. Simon 2019; E. Sacchi et al. 2021; C. Gallart et al. 2021; J. D. Simon et al. 2021; K. B. W. McQuinn et al. 2023; A. Savino et al. 2023; J. D. Simon et al. 2023; D. R. Weisz et al. 2023; K. B. W. McQuinn et al. 2024). The observed properties of UFDs support theoretical ideas that galaxy growth in the lowest-mass halos is limited or entirely suppressed by a combination of supernova feedback and the ultraviolet (UV) background radiation resulting from cosmic reionization, which not only heats and expels halo gas, but also prevents the cooling and inflow of fresh gas from the surrounding intergalactic medium (e.g., G. Efstathiou 1992; J. S. Bullock et al. 2000; R. S. Somerville 2002; A. J. Benson et al. 2002, 2003; M. S. Bovill & M. Ricotti 2009; J. A. Muñoz et al. 2009; S. Salvadori & A. Ferrara 2009; M. T. Busha et al. 2010; J. Tumlinson 2010; C. M. Simpson et al. 2013; C. Wheeler et al. 2015; M. Jeon et al. 2017; H. Katz et al. 2020). This limitation, driven by the interplay of internal and external feedback, in turn, is an important mechanism needed to reproduce galaxy counts at the low-mass regime within cold dark matter cosmological models (e.g., T. Sawala et al. 2016; A. R. Wetzel et al. 2016; C. M. Simpson et al. 2018; T. Buck et al. 2019; S. Garrison-Kimmel et al. 2019; A. S. Font et al. 2021; C. Engler et al. 2021).

Cosmic reionization is thought to be a highly inhomogeneous process (e.g., S. R. Furlanetto et al. 2006; L. Pentericci et al. 2014; G. D. Becker et al. 2015; A. D’Aloisio et al. 2015; K. M. Smith & S. Ferraro 2017; S. Ferraro & K. M. Smith 2018; X. Jin et al. 2024). Regions with the highest density were reionized first, while those with lower density, which could include field galaxies, the outskirts of the proto-Local Group or isolated proto-Large Magellanic Cloud (LMC)-mass groups, were ionized later, allowing prolonged star formation in low-mass

halos (e.g., S. R. Furlanetto et al. 2004; M. McQuinn et al. 2007; B. E. Robertson et al. 2010; E. Sobacchi & A. Mesinger 2013; R. Endsley et al. 2021; O. Zier et al. 2025). Various simulations suggest that the expected reionization time difference among progenitors of MW or M31-size galaxies is expected to be 200-500 Myr (e.g., R. Lunnan et al. 2012; T. Y. Li et al. 2014; D. Aubert et al. 2018; T. Dawoodbhoj et al. 2018; H. Zhu et al. 2019; H. Katz et al. 2020; P. Ocvirk et al. 2020; J. G. Sorce et al. 2022; J. Kim et al. 2023; Y. Zhao et al. 2025). However, the impact of patchy reionization on low-mass galaxies, particularly in the context of surviving satellites of individual MW-mass halos, has not been studied as thoroughly due to computational limitations.

Unfortunately, our ability to conduct detailed, empirical characterizations of the impact of reionization on the formation of UFDs remains limited. UFDs are generally too faint to be directly detected beyond the very local Universe, and our ability to place their formation history into a cosmological context is largely limited to the Local Group. Within the Local Group, detailed color-magnitude diagram (CMD)-based star formation histories (SFHs) have the potential to reveal early Universe signatures, such as patchy reionization. However, to date they have been restricted to small samples, primarily in the halo of the Milky Way (MW, e.g., D. R. Weisz et al. 2012, 2014a; T. M. Brown et al. 2014; E. Sacchi et al. 2021; J. D. Simon et al. 2023; C. T. Garling et al. 2024).

It is only recently that studies have begun to explore how the duration and decline of star formation in UFDs varies across stellar mass and galaxy environment (E. Sacchi et al. 2021; K. B. W. McQuinn et al. 2023; A. Savino et al. 2023). Furthermore, precise proper motions (PMs) measured by the *Gaia* mission have provided a novel opportunity to probe the environmental dependence of UFD’s early evolution. By using *Gaia* PM-based orbital histories, the MW UFDs have been classified into 3 kinematic groups (e.g., T. K. Fritz et al. 2018; N. Kallivayalil et al. 2018; E. Patel et al. 2020; A. B. Pace et al. 2022). The first is made of UFDs that are likely on their first infall into the MW’s halo. The second contains UFDs consistent with being long-term MW satellites. The third consists of UFDs associated with the LMC group. The LMC is thought to be on its first approach to the MW (e.g., G. Besla et al. 2007; N. Kallivayalil et al. 2013), bringing its satellites—the Small Magellanic Cloud (SMC) and potentially a num-

* NASA Hubble Fellow

ber of UFDs—with it. Gaia PMs indicate that 4 of the known UFDs (Carina I, Carina II, Horologium I, and Hydrus I) are highly likely satellites of the LMC, and Phoenix II and Reticulum II are also suspected companions based on their position, distance, and orbital properties (L. V. Sales et al. 2017; N. Kallivayalil et al. 2018; E. Patel et al. 2020).

While we acknowledge the complexity in reconstructing the early environments of surviving satellites (e.g., A. R. Wetzel et al. 2015; I. B. Santistevan et al. 2023), the different categories of UFD orbital histories in the MW halo mean that their ancient SFHs may carry the imprint of the different environmental conditions they might have experienced early in their evolution. Thus, despite the limitations of current information, examining the kinematic group context of UFDs can still provide valuable insights into possible environmental influences on their early evolutionary pathways. For instance, by analyzing deep *HST* imaging, E. Sacchi et al. (2021) measured a difference of ~ 600 Myr between the average quenching time of 3 UFDs associated with the LMC and those of 4 other UFDs. This work demonstrates how one might probe the inhomogeneity of reionization over co-moving volumes of ~ 350 Mpc³ (M. Boylan-Kolchin et al. 2016) by quantifying the differences in SFH and quenching among MW UFDs, and by identifying their early environments by means of orbital reconstruction.

A robust characterization of these subtle differences in such ancient stellar populations requires careful mitigation of both statistical and systematic uncertainties. The sparse stellar populations of these low-mass galaxies can result in statistically uncertain quenching times on a per-object basis (T. M. Brown et al. 2014). On the other hand, systematic inhomogeneities in photometric reduction, stellar models, and/or distance determination that can stem from collating literature results can easily confound the signal encoded in the SFHs. The best approach is therefore to analyze a large sample of galaxies using a homogeneous methodology.

In this paper, we uniformly reduce and analyze all public deep *HST* ACS/WFC optical imaging that has targeted the oldest main sequence turn-off (oMSTO) of 36 UFDs in the Local Group. We produce photometric catalogs, derive homogeneous distances, and measure the SFHs using consistent methodology. We use this dataset to analyze the formation and quenching of UFDs in the early Universe, with an emphasis on exploring putative differences within the UFD population as a function of kinematical association.

While there have been efforts toward the homogeneous analysis of deep *HST* imaging in the Local Group (e.g.,

C. Gallart & LCID Team 2007; T. M. Brown et al. 2014; D. R. Weisz et al. 2014b; E. Sacchi et al. 2021; A. Savino et al. 2025), most dwarf galaxies within ~ 1.5 Mpc have been the subject of small-sample studies, often with meaningful methodological differences between them, and/or include data of heterogeneous quality, which can introduce additional systematics (e.g., D. R. Weisz et al. 2011a; C. Gallart et al. 2021; J. D. Simon et al. 2021, 2023; D. R. Weisz et al. 2023). In this paper, we make a step forward by providing a homogeneous photometric dataset that covers all MW UFDs with contemporary, deep *HST* data. In future papers, we will expand our work by re-analyzing a larger number of galaxies, increasing the diversity of masses, morphologies, and environments in our database using a uniform approach across the entire sample. The high-level science products (HLSPs) produced by this program are hosted on MAST and can be accessed at the URL <https://archive.stsci.edu/hlsp/laurelin/> or by DOI: 10.17909/b8yw-wv58.

This paper is organized as follows. In section 2 we provide an overview of our dataset and of the photometric reduction. In section 3 we detail our procedure for measuring the SFHs and quantifying the star formation quenching timescales. In section 4 we compare our results to past empirical studies and theoretical predictions, and make recommendations for future work. In section 5 we present our conclusions.

2. OBSERVATIONS AND DATA REDUCTION

2.1. Sample

Our sample comprises 36 UFDs with deep *HST* ACS/WFC imaging in F606W and F814W ($S/N > 50$ at the oMSTO in all cases, $S/N > 100$ in most), spanning an absolute V magnitude range of $-7.1 \leq M_V \leq +0.0$. The size-magnitude parameter space of our sample is shown in Figure 1.

We note that while most of the UFDs in this analysis have been confirmed spectroscopically or are too large to be globular clusters, there are three systems whose classifications remain uncertain: Eri III, Sag II, and Tuc III (N. Longeard et al. 2021; S. W. Fu et al. 2023; J. D. Simon et al. 2024; D. Zaremba et al. 2025). Of these, Sag II is the most likely to be a cluster based on its very low mass-to-light ratio and minimal metallicity dispersion (N. Longeard et al. 2021). We retain these objects in our overall sample and in calculations that include the full sample, and refer to them as UFDs throughout regardless, but exclude Sag II from certain parts of the later analysis that are restricted to a high-quality subsample.

Table 1. Observations

Galaxy	Abbrev.	t_{exp} [ks]		$m_{50\%}$ [Vegamag]		S/N _{MSTO}	f_{\star}^a	$M_{V\text{eff}}^b$	Tiles	Proposal IDs
		F606W	F814W	F606W	F814W					
Boötes I	Boo I	41.1	41.2	27.58	26.94	335	0.14	−3.89	5	12549, 15317
Boötes II	Boo II	9.2	9.2	27.43	26.76	427	0.35	−1.81	2	14734
Canes Venatici II	CVn II	31.6	20.9	28.46	27.84	269	0.63	−4.66	1	12549, 14236
Cetus II	Cet II	4.6	4.6	27.35	26.74	683	0.50	0.75	1	14734
Columba I	Col I	4.7	4.7	27.47	26.83	81	0.39	−3.18	1	14734
Coma Berenices	ComBer	98.6	65.8	27.45	26.82	493	0.58	−3.68	12	13449, 12549
Draco II	Dra II	4.7	4.7	27.39	26.74	874	0.29	0.53	1	14734
Eridanus II	Eri II	12.8	28.6	28.04	27.42	55	0.55	−6.45	1	14234, 14224
Eridanus III	Eri III	4.6	4.6	27.41	26.74	198	0.96	−2.03	1	14734
Grus I	Gru I	4.8	4.8	27.48	26.84	139	0.59	−2.90	1	14734
Grus II	Gru II	4.6	4.6	27.43	26.81	344	0.10	−1.45	1	14734
Hercules	Her	69.3	60.0	28.18	27.51	234	0.23	−4.23	4	12549, 14236, 15182
Horologium I	Hor I	4.6	4.6	27.48	26.83	218	0.55	−3.11	1	14734
Horologium II	Hor II	9.3	9.3	27.53	26.92	235	0.58	−0.97	2	14734
Hydra II	Hya II	4.7	5.8	27.37	26.76	114	0.58	−4.27	1	14734, 14224
Hydrus I	Hyi I	2.2	2.6	26.51	25.91	258	0.14	−2.54	2	16293
Leo IV	Leo IV	30.9	20.5	28.28	27.66	253	0.25	−3.49	1	12549, 14236
Leo V	Leo V	4.6	4.6	27.21	26.58	86	0.75	−3.98	1	14770
Pegasus III	Peg III	4.7	4.7	27.25	26.58	68	0.47	−3.29	1	14734
Phoenix II	Phe II	4.6	4.6	27.41	26.76	195	0.53	−2.01	1	14734
Pictor I	Pic I	4.8	4.8	27.47	26.80	139	0.80	−3.43	1	14734
Pisces II	Pisc II	4.7	4.7	27.39	26.74	88	0.71	−3.87	1	14734
Reticulum II	Ret II	16.4	18.3	26.77	26.11	346	0.59	−3.30	12	14734, 14766
Reticulum III	Ret III	4.7	4.7	27.38	26.72	178	0.42	−2.36	1	14734
Sagittarius II	Sag II	4.6	4.6	27.20	26.58	272	0.59	−4.63	1	14734
Segue 1	Seg 1	9.2	9.2	27.35	26.71	621	0.30	−0.01	2	14734
Segue 2	Seg 2	4.6	4.6	27.37	26.74	430	0.20	−0.24	1	14734
Triangulum II	Tri II	9.2	9.2	27.31	26.67	576	0.47	−0.79	2	14734
Tucana II	Tuc II	17.5	18.6	27.44	26.79	332	0.22	−2.25	4	14734
Tucana III	Tuc III	9.3	9.3	27.42	26.76	777	0.19	0.29	2	14734
Tucana IV	Tuc IV	9.3	9.3	27.48	26.85	419	0.08	−0.79	2	14734
Tucana V	Tuc V	4.7	4.7	27.46	26.84	339	0.43	−0.67	1	14734
Ursa Major I	UMa I	45.9	33.5	27.56	26.92	184	0.31	−3.86	9	12549, 14236
Ursa Major II	UMa II	9.3	9.3	27.45	26.78	523	0.05	−1.11	2	14734
Virgo I	Vir I	2.4	2.3	26.97	26.33	145	0.59	−0.23	1	15332
Willman 1	Wil 1	4.6	4.6	27.42	26.78	427	0.35	−1.77	1	14734

^a The fraction of the galaxy’s integrated light within the *HST* footprint, calculated using the profiles shown in Figure 2.

^b The effective integrated *V* magnitude of the *HST* pointing, $M_{V\text{eff}} = M_V - 2.5 \log_{10}(f_{\star})$.

Our full set of new and archival observations are summarized in Table 1, and footprints of all pointings overlaid with galaxy profiles are shown in Figure 2. The new data comprises two pointings in Hydrus I (GO-16293,

PI Choi),¹⁷ and the bulk of the archival data comes from programs GO-14734 (PI Kallivayalil, 26 galaxies)

¹⁷ GO-16293 also observed three fields in Carina II, but the central pointing experienced a guide star failure and was not re-observed. We elected not to include the remaining two fields in this work, as we found they were too sparse to be of use for the goals of this paper.

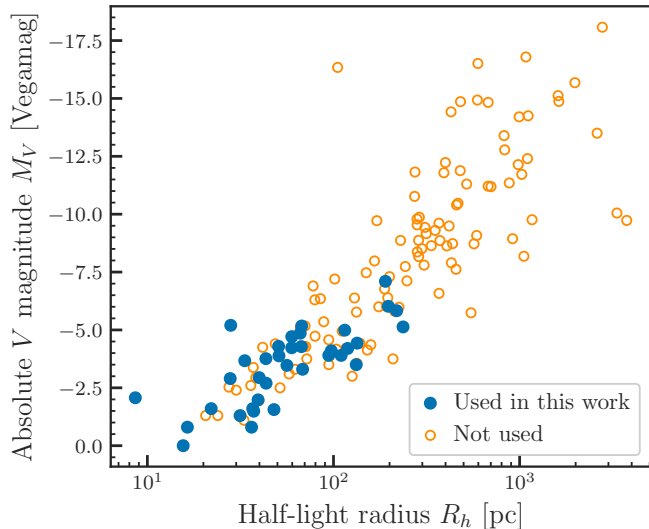


Figure 1. Size-magnitude relation for known Local Group dwarf galaxies within 1.5 Mpc. Filled blue points are the galaxies used in this work, and open orange circles are other local galaxies not studied here, either because they are too massive to be considered UFDs or because they lack *HST* imaging. Data obtained from the Local Volume Database (A. B. Pace 2024).

and GO-12549 (PI Brown, 6 galaxies). Other archival programs include GO-13449 (PI Geha), GO-14224 (PI Gallart), GO-14234 (PI Simon), GO-14236 (PI Sohn), GO-14766 (PI Simon), GO-14770 (PI Sohn), GO-15182 (PI Sand), GO-15317 (PI Platais), and GO-15332 (PI Crnojevic).

Following A. Savino et al. (2025) we quantify the fraction of a galaxy’s total light expected to fall within the *HST* pointing(s) as f_* , which we estimate using surface brightness profiles. From this and M_V we calculate $M_{V\text{eff}}$, the effective magnitude of the *HST* observations, $M_V - 2.5 \log_{10}(f_*)$. We adopt structural parameters from the exponential profile fitting results of R. R. Muñoz et al. (2018) where available, with the following exceptions: Cet II & Ret III (A. Drlica-Wagner et al. 2015); Col I (J. L. Carlin et al. 2017); Dra II (B. P. M. Laevens et al. 2015); Gru II, Tuc IV, & Tuc V (J. D. Simon et al. 2020); Hyi I (S. E. Kuposov et al. 2018); Peg III (H. Richstein et al. 2022); Sag II & Tuc III (B. Mutlu-Pakdil et al. 2018); Tuc II (K. Bechtol et al. 2015); and Vir I (D. Homma et al. 2016).

2.2. Astrometric alignment

We adopt a modified version of the workflows described in V. Bajaj (2017)¹⁸ and V. Bajaj & J. Ander-

son (2020)¹⁹ to align our *HST* exposures with *TweakReg*. *TweakReg* is a routine included in the *Drizzlepac* software package (S. Gonzaga et al. 2012; STSCI Development Team 2012; R. J. Avila et al. 2015; S. L. Hoffmann et al. 2021) that derives transformations between coordinates of sources in a reference frame and sources in individual exposures using a triangle pattern matching algorithm, and optionally updates the exposure headers’ WCS information with the “tweaked” astrometric solutions. Although absolute alignment to the *Gaia* DR3 reference frame is preferred for sufficiently populated images, a number of observations have few or no *Gaia* sources within their footprints. Therefore we perform only relative alignment on a per-target basis.

We measured input exposure-level catalogs with the *hst1pass* software (J. Anderson 2022) for use as *TweakReg* inputs. *hst1pass* is a publicly available FORTRAN routine designed to measure precise astrometry and photometry of relatively bright, isolated stars in individual *HST* *flt* or *flc* frames using effective point spread function fitting (ePSF, J. Anderson & I. R. King 2000, 2006). With these we fit shifts, rotation, and scale relative to the deepest exposure for all exposures in a stack. The median RMS of the residuals is under 0.05 pixels, or 2.5 mas. We then combined the aligned images to create a deep undistorted reference image for each target with *AstroDrizzle* (A. S. Fruchter & R. N. Hook 2002) with the parameters recommended for ACS in the Hubble Advanced Products pipeline (HAP, J. Mack et al. 2022).

We provide all drizzled reference images as part of our data release.

2.3. Photometry

We measured full-stack photometry on the aligned images using the DOLPHOT package (A. E. Dolphin 2000; A. Dolphin 2016). We largely follow the input parameter recommendations of the PHAT (B. F. Williams et al. 2014, 2023) and PHATTER (B. F. Williams et al. 2021) surveys, with the following exceptions:

1. We turn DOLPHOT’s internal alignment step off with `Align=0`. In combination with `UseWCS=2`, this ensures that the *hst1pass*-derived astrometric solutions described in the previous section are used as-is.
2. Following A. Savino et al. (2023), we add a second iteration of PSF fitting with `PSFPhotIT=2`, which improves noise estimates in the final photometric solution. (Note that this is distinct from

¹⁸ https://github.com/spacetelescope/gaia_alignment/

¹⁹ https://github.com/spacetelescope/wfc3_photometry/

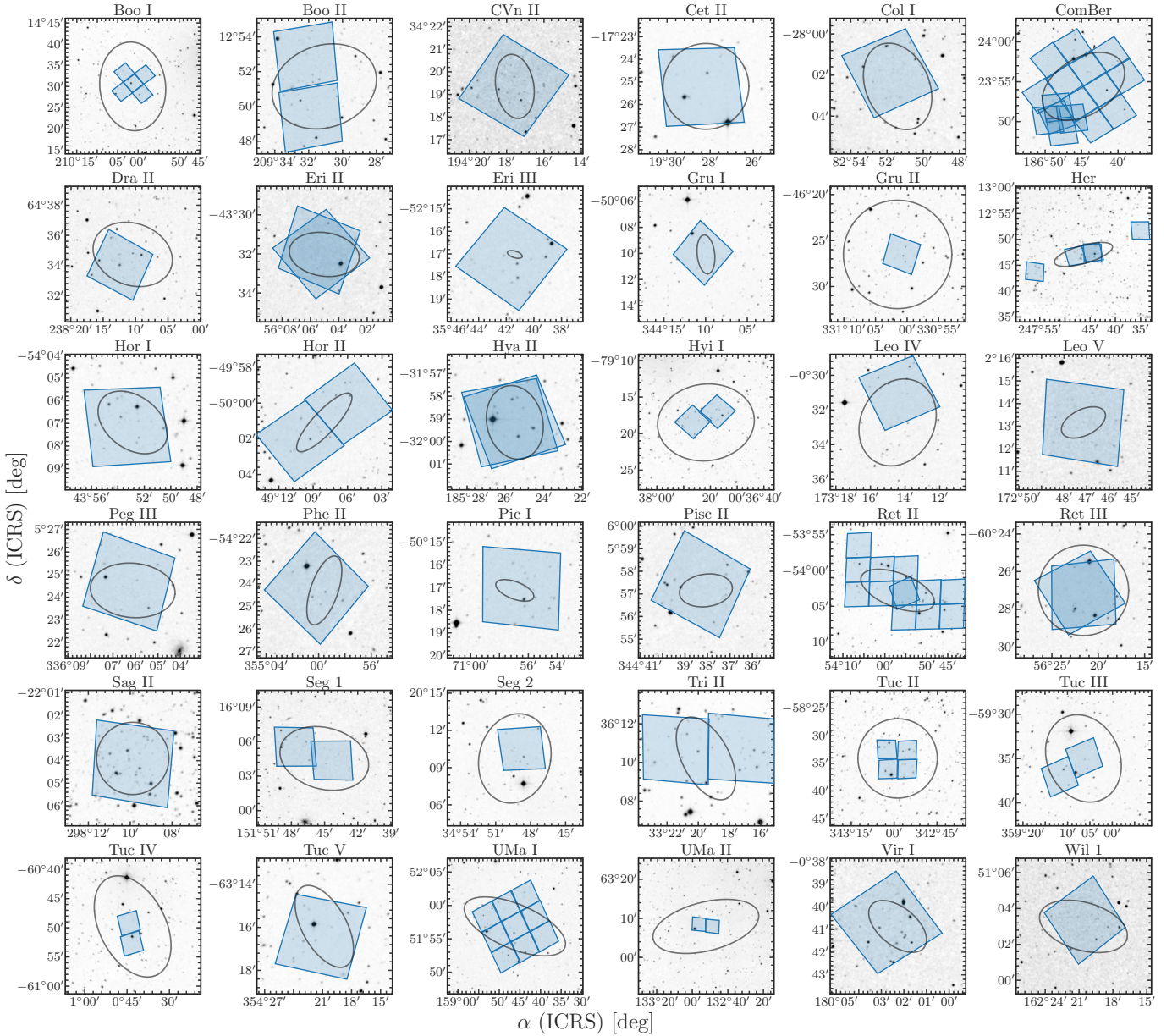


Figure 2. Footprints of all *HST* observations used in this work (blue filled patches) overlaid on DSS2 imaging cutouts. Open black ellipses show the galaxy profiles at one half-light radius.

the number of star-finding iterations, which is set by `SecondPass`.)

We adopt somewhat stricter quality cuts on our photometry than the GST (“good star”) cuts applied to PHAT & PHATTER, as our data have much lower crowding. These cuts, applied per filter, are:

- $S/N \geq 4$
- $\text{Sharpness}^2 \leq 0.2$
- $\text{Crowding} \leq 0.75$
- $\text{Roundness} \leq 0.3$

- $\text{Flag} \leq 3$

We then impose further quality criteria on the sharpness, roundness, and crowding values by combining the filter-level quantities. We add the per-filter sharpness and roundness values in quadrature, and convert the crowding values from magnitude to fractional flux before taking their average and converting back to magnitudes to arrive at global values per source. We apply a modified version of the culling technique explored by [J. J. Dalcanton et al. \(2015\)](#), who rejected low-quality measurements by fitting ellipses to two-dimensional dis-

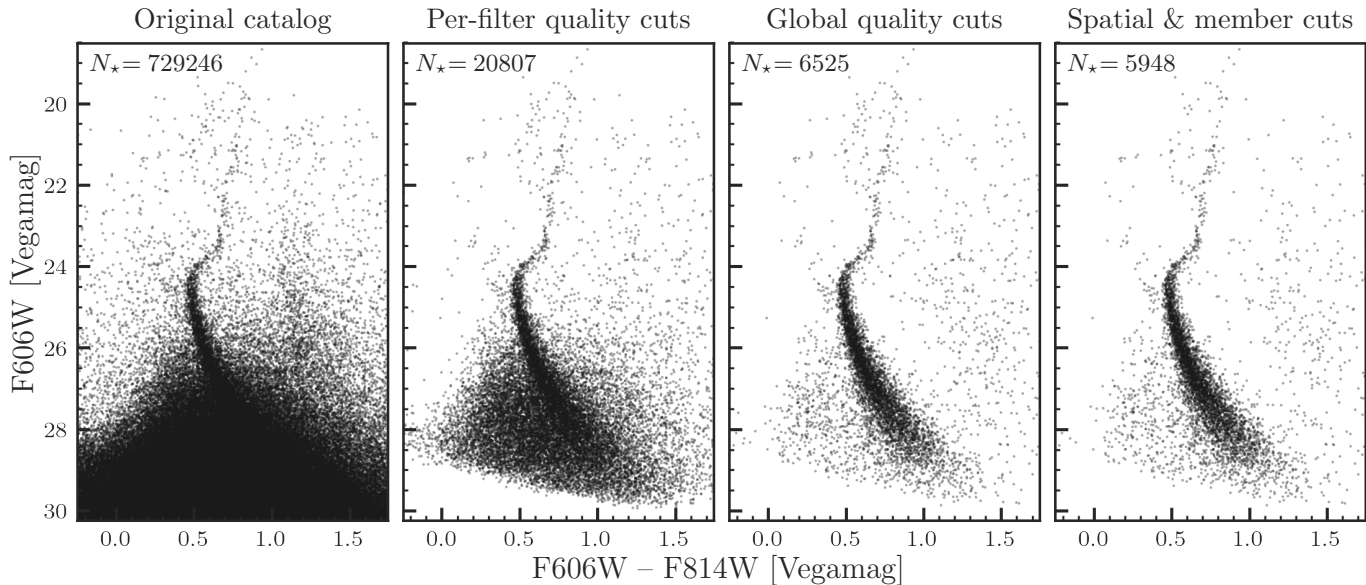


Figure 3. Application of successive culling criteria to CMDs of Hercules, with the fourth panel showing the final version of the catalog used in the remainder of this work. The stellar population signal of the galaxy remains constant throughout, whereas noise, artifacts, and contaminant populations are dramatically reduced.

tributions of the aforementioned quality metrics. In our case, we require:

- $\text{Sharpness}^2 + \text{Roundness}^2 + \text{Crowding}^2 < 0.1$
- $|\text{Sharpness} \times \text{Roundness} \times \text{Crowding}| < 0.001$

In our uncrowded, high S/N data, these fairly strict cuts produce CMDs with substantially reduced populations of background galaxies and artifacts such as shredded diffraction spikes of saturated stars, while maintaining high completeness for the bona-fide stellar sources, as demonstrated in Figure 3 and Figure 4. Some galaxies, most notably Her, Boo I, UMa I, ComBer, and Ret II, still show residual populations of unrejected background galaxies at faint magnitudes bluewards of the main sequence; the prominence of this feature generally correlates with the total area observed, and is accounted for in our CMD modeling procedure as described in the next section.

We reject likely foreground stars based on the membership determinations of G. Battaglia et al. (2022), which combine *Gaia* eDR3 proper motions with spatial and color-magnitude information. We keep only stars with $P_{\text{memb}} \geq 0.75$ for stars with membership probabilities. We also restrict the input catalogs to stars within two half-light radii of each target using the structural parameters compiled in their Table B.1. For Pic I and Peg III we extend the selection to $2.5R_h$, and for Eri III to $3R_h$, as we see significant stellar population signal out to these radii in these galaxies. We additionally reject stars within $2R_h$ of the globular cluster in Eri II based

on the structural parameters reported by J. D. Simon et al. (2021).

We demonstrate the application of all quality and membership criteria in Hercules in Figure 3, and show color-magnitude diagrams of the final culled photometry for all galaxies in Figure 4 and Figure 5. Figure 4 shows nearly the full dynamic range of the photometry for all galaxies in apparent magnitudes, and Figure 5 is restricted to ± 2 magnitudes around the MSTO in absolute magnitudes. We provide the full set of photometric catalogs (e.g., inclusive of all stars regardless of quality, but with columns indicating whether quality criteria are met) as part of our data release.

2.4. Artificial star tests

We assess photometric completeness, bias, and scatter for each galaxy using artificial star tests (ASTs), with 100,000 artificial stars per exposure depth per target. The ASTs are distributed uniformly in color and magnitude, and their locations on the field of view follow the spatial distributions of observed stars. Artificial stars are injected into the images one at a time and measured identically to the photometry described in the previous subsection, with the exception of the parameter `ACSUseCTE`. Although we used CTE-corrected `*_flc` images throughout, for the artificial stars we set `ACSUseCTE=1` to ensure realistic evaluation of the photometric noise induced by CTE correction, which is not otherwise accounted for in DOLPHOT’s AST routine. All the same photometric quality metrics and spatial

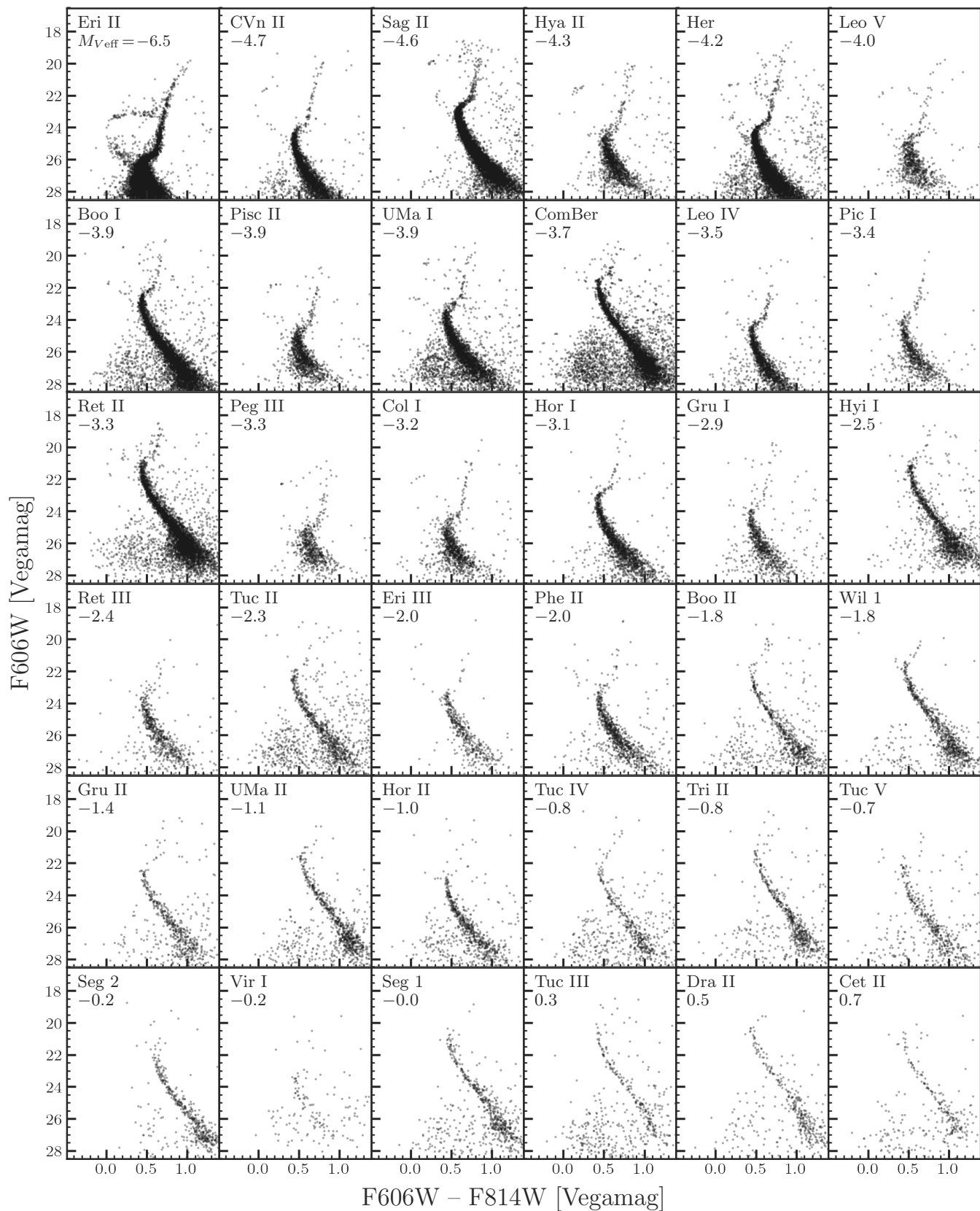


Figure 4. Color-magnitude diagrams of all galaxies, with all photometric quality and membership cuts applied. The integrated magnitudes in each panel reflect the effective luminosity, i.e., the luminosity within *HST*'s field of view for each galaxy.

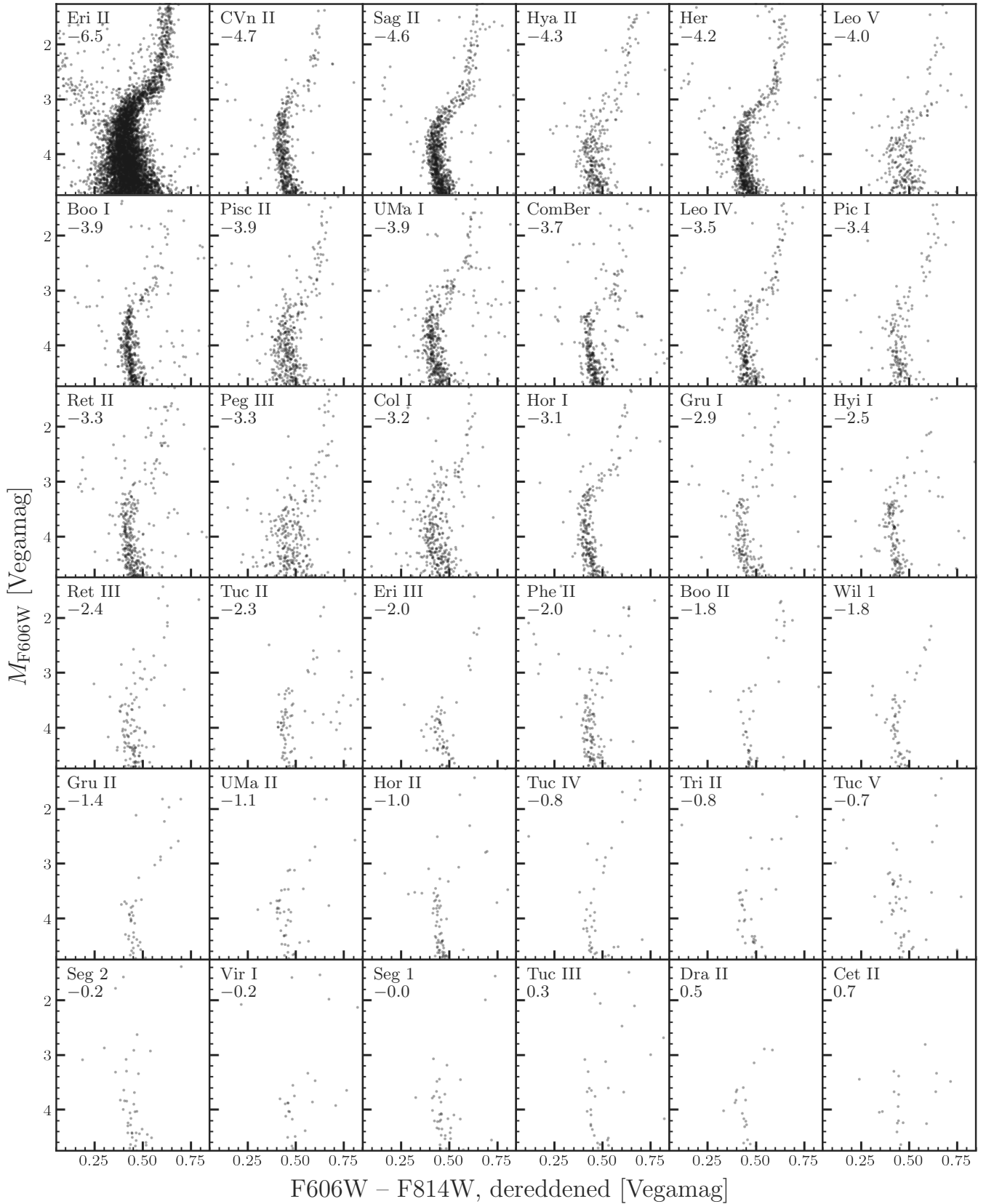


Figure 5. As Figure 4, but using absolute magnitudes (based on the distances and reddenings reported in Table 2) and zooming in on the few magnitudes around the oMSTO, subgiant branch, and base of the red giant branch.

culling used on the real catalogs are applied to the artificial star photometry outputs.

3. STAR-FORMATION HISTORIES

In this section we present SFHs of all 36 galaxies. We first measure distance and foreground extinction values for each galaxy via main sequence fitting (detailed in subsection 3.1), and then discuss their SFH fitting process and results (subsection 3.3). We perform all SFH fitting with *MATCH* (A. E. Dolphin 2002), a well-tested software package frequently used in resolved stellar populations studies (e.g., E. D. Skillman et al. 2003; B. F. Williams et al. 2009; K. B. W. McQuinn et al. 2010; M. Monelli et al. 2010; D. R. Weisz et al. 2011b, 2014b; A. R. Lewis et al. 2015; K. B. W. McQuinn et al. 2015; E. D. Skillman et al. 2017; A. Savino et al. 2023, 2025). *MATCH* measures a maximum-likelihood SFH solution by comparing observed and modeled Hess diagrams via Poisson statistics.

3.1. Distances and foreground extinctions

While most, if not all, of our sample have at least one distance measurement available in the literature, they vary greatly in method and precision. Similarly, foreground extinctions reported by different dust maps (e.g., D. J. Schlegel et al. 1998; G. M. Green et al. 2019; R. Lallement et al. 2022; L. Delchambre et al. 2023) differ by up to 0.3 mag in A_V for the same galaxy. The heterogeneity of these values, and their adoption in the literature, can affect the inferred stellar populations of each system.

Therefore, we choose to measure self-consistent distances and extinctions for each galaxy by fitting them as simple stellar populations (SSPs) between the base of the red giant branch and the main sequence knee (approximately $2 < M_{F606W} < 6$ as shown in Figure 5). For this we use the *MATCH* SSP fitting utility, which performs a grid search over specified ranges of distance, extinction, age, and metallicity for single-age, single-metallicity populations (SSPs).

We use the BaSTI (A. Pietrinferni et al. 2004; S. L. Hidalgo et al. 2018) stellar model suite (A. Pietrinferni et al. 2021) to generate fiducial SSP isochrones. We use BaSTI throughout this work because it is the only model suite available in *MATCH* that covers the extremely low metallicities and alpha abundance ratios found in UFDs. We choose grids of $10 < \log_{10}(t/\text{yr}) < 10.14$ (10 - 13.8 Gyr) with 0.01 dex steps and $-3.2 \leq [\text{Fe}/\text{H}] \leq -1.4$ with 0.1 dex steps, with $[\alpha/\text{Fe}] = 0.4$. For distances we set a range of ± 0.4 mag around the literature distance moduli compiled in G. Battaglia et al. (2022) with 0.01 mag steps. For extinction, we take the A_V values reported by

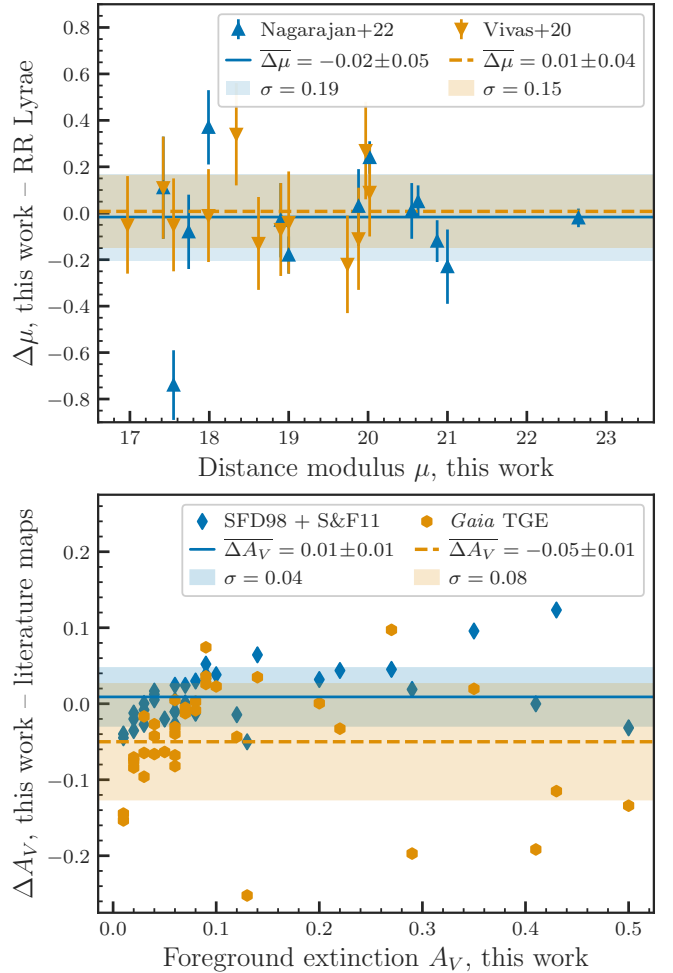


Figure 6. Comparisons of our SSP-based distance and extinction measurements with literature values. Upper panel: comparison of our distance moduli with RR Lyrae results from P. Nagarajan et al. (2022, blue triangles) and A. K. Vivas et al. (2020, orange inverted triangles). Error bars reflect only the RR Lyrae distances’ uncertainties, as we do not calculate formal uncertainties on ours. Average differences between respective distance moduli are shown as horizontal lines, and standard deviations as horizontal bars. Lower panel: comparison of our A_V with values from the maps of D. J. Schlegel et al. (1998, blue diamonds), with R_V from E. F. Schlafly & D. P. Finkbeiner (2011), and L. Delchambre et al. (2023, orange hexagons). As above, averages and standard deviations are marked with horizontal lines and bars.

the respective all-sky maps of D. J. Schlegel et al. (1998) (recalibrated by E. F. Schlafly & D. P. Finkbeiner 2011) and L. Delchambre et al. (2023) as starting points, and set the lower limit to 0.05 mag below the minimum of the two values, and the upper limit to 0.05 mag greater than the maximum, with 0.01 mag steps. We report all best-fit distance moduli μ and foreground extinctions A_V in Table 2, as well as ages and metallicities.

Table 2. Best-fit SSP parameters

Galaxy	A_V [mag]	μ [mag]	$\log(t/\text{yr})$	[Fe/H]
Boo I	0.01	19.00	10.11	-2.0
Boo II	0.06	18.34	10.10	-2.5
CVn II	0.04	21.00	10.13	-2.8
Cet II	0.06	17.25	10.11	-2.5
Col I	0.06	21.22	10.12	-2.3
ComBer	0.01	17.99	10.11	-2.0
Dra II	0.09	16.58	10.12	-2.1
Eri II	0.03	22.65	10.08	-1.7
Eri III	0.06	19.74	10.09	-2.4
Gru I	0.04	20.55	10.12	-2.6
Gru II	0.07	18.69	10.12	-2.0
Her	0.22	20.63	10.13	-2.6
Hor I	0.02	19.66	10.13	-2.7
Hor II	0.03	19.42	10.12	-2.3
Hya II	0.20	20.68	10.12	-1.6
Hyi I	0.35	17.42	10.12	-2.9
Leo IV	0.05	20.87	10.13	-2.0
Leo V	0.14	21.09	10.09	-1.6
Peg III	0.41	21.25	10.09	-1.5
Phe II	0.06	19.88	10.11	-3.0
Pic I	0.03	20.54	10.13	-2.9
Pisc II	0.13	21.14	10.11	-1.9
Ret II	0.08	17.57	10.12	-3.1
Ret III	0.12	19.97	10.10	-2.5
Sag II	0.43	18.90	10.12	-1.9
Seg 1	0.08	17.12	10.10	-1.8
Seg 2	0.50	17.74	10.11	-2.1
Tri II	0.27	17.50	10.10	-2.8
Tuc II	0.02	18.62	10.12	-2.2
Tuc III	0.02	16.97	10.09	-2.7
Tuc IV	0.04	18.41	10.11	-2.6
Tuc V	0.10	18.89	10.11	-2.9
UMa I	0.09	20.02	10.10	-2.9
UMa II	0.29	17.55	10.11	-2.1
Vir I	0.07	19.68	10.11	-1.9
Wil 1	0.09	17.93	10.13	-3.0

We compare our derived distances to those measured from RR Lyrae variable stars calibrated to *Gaia* in the upper panel of Figure 6. P. Nagarajan et al. (2022) recalibrated literature RR Lyrae measurements in 39 Local Group dwarfs, including 13 of the UFDs analyzed here, to anchor them to the *Gaia* Milky Way RR Lyrae period-luminosity-metallicity relation. A. K. Vivas et al. (2020) used *Gaia* DR2 data to identify and measure distances to RR Lyrae in 14 nearby UFDs, 12 of which are in our sample. Of these, 7 galaxies are common be-

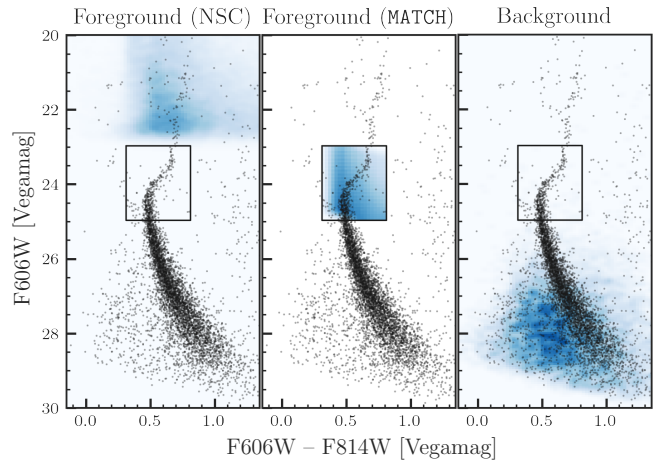


Figure 7. Example foreground and background components for Hercules, shown as blue density maps with scatter plots of the CMD overlaid. The color-magnitude box we use for SFH fitting is outlined in black on each panel. In this case, the NOIRLab Source Catalog (NSC, left panel) is too shallow to reach Hercules’ MSTO, so that foreground component has a weight of zero in the resulting SFH fit, and the MATCH foreground model (center panel) is used instead. However, this is not the case for all galaxies. Similarly, the background component (right panel) is negligible here, but in more distant galaxies it carries more weight.

tween the two studies, for a total of 18 individual galaxies or half our total sample. We find small mean offsets ($|\overline{\Delta\mu}| \leq 0.02$ mag) between our distances and the RR Lyrae results (horizontal lines in Figure 6), albeit with high scatter (~ 0.2 mag, shaded horizontal bars) around the mean. The outlier at $\Delta\mu = -0.75$ is UMa II, whose RR Lyrae distance is based on a single RRab star, and for which P. Nagarajan et al. (2022) note comparable discrepancies between their measurement and prior literature distances. In general, our distances are in good agreement with the literature, and have the benefit of uniformity.

3.2. Foreground & background populations

MATCH offers the option to include components in the likelihood that represent foreground Galactic populations as well as unresolved background galaxies and other non-stellar sources in the CMD fitting process. In our sparsely populated data, even a small number of spurious sources can affect the CMD fits and resulting SFHs. Therefore, accurately modeling all non-UFD components is essential.

For the Galactic foreground we supplement the built-in MATCH foreground model, which implements a smooth three-component Milky Way profile (J. T. A. de Jong et al. 2010), with *ri* photometry from Pan-STARRS DR1 (PS1, K. C. Chambers et al. 2016; H. A. Flewelling

et al. 2020) or the NOIRLab Source Catalog DR2 (NSC, D. L. Nidever et al. 2018, 2021) depending on availability. We query the respective catalogs within an annulus around each galaxy, starting at $6R_h$ and extending to $10R_h$ or 0.5° , whichever is larger. The PS1 and NSC catalogs reach typical limiting r -band magnitudes of approximately 21 and 23 respectively, which cover the oMSTO for only the nearest \sim half of the galaxy sample. However, they may be informative as to any coincident Galactic halo substructures (as in the case of, e.g., Gru II and the Chenab/Orphan Stream, C. E. Martínez-Vázquez et al. 2019). We convert the ri magnitudes from their native AB system to the Vega system, but do not apply any additional color transformations to put them on the HST filter system, as the background structures are intrinsically diffuse in color-magnitude space over the narrow color range of interest, and convolved with a smoothing kernel in MATCH (see subsection 3.3 and Figure 7).

For the background, we use the subset of culled photometry that meets the per-filter GST quality cuts but fails the global quality cuts. These largely consist of unresolved background galaxies and shredded diffraction spikes from saturated foreground stars. We allow a linear scaling factor for all foreground and background components to vary freely in the CMD fitting. We illustrate all foreground and background components against the final fitted CMD for Hercules in Figure 7.

3.3. CMD fits

With distances, extinctions, and all foreground and background components in hand, we generate stellar population models with ages between $9.78 \leq \log_{10}(t/\text{yr}) < 10.14$ (6 – 13.8 Gyr) with an 0.01 dex step size, and metallicities between $-3.2 < [\text{Fe}/\text{H}] < -1.2$ with an 0.1 dex step, again using the BaSTI model suite with $[\alpha/\text{Fe}] = 0.4$. We use a Kroupa initial mass function (P. Kroupa 2001) normalized between $0.08 M_\odot$ and $120 M_\odot$, an unresolved binary fraction of 0.35, and bin sizes of 0.025, 0.05 mag in color and magnitude respectively. Following previous analyses of Local Group dwarfs (e.g., D. R. Weisz et al. 2014a; E. D. Skillman et al. 2017; A. Savino et al. 2023), we impose an age-metallicity relation constraint using the `-zinc` option, which specifies that the mean metallicity must increase monotonically over time. This option mitigates the age-metallicity degeneracy at the oMSTO, particularly for the metallicity-insensitive F606W-F814W filter combination (A. Savino et al. 2023). We allow the initial metallicity to vary between $-3.2 \leq [\text{Fe}/\text{H}] \leq -2.0$ dex, and the final between $-3.2 \leq [\text{Fe}/\text{H}] \leq -1.6$ dex. We additionally set a metallicity dispersion of

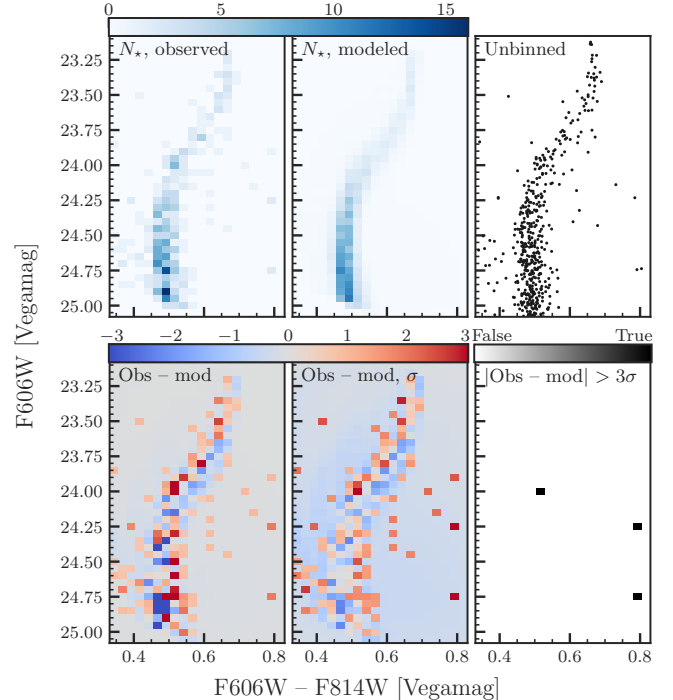


Figure 8. Example MSTO fitting for Hercules. Upper row, left to right: observed and modeled Hess diagrams, and the unbinned CMD for reference. Lower row: Hess diagram residuals (observed – modeled) and residual significance, and bins with residual significance over 3σ . The complete figure set (36 images) is available in the online journal.

$\langle \sigma_{[\text{Fe}/\text{H}]} \rangle = 0.2$ dex per age bin (E. N. Kirby et al. 2011; I. Escala et al. 2018).

We set the default magnitude range for the CMD fitting to within ± 1 mag of the oMSTO ($2.5 \leq M_{\text{F606W}} \leq 4.5$); for galaxies with fewer than 100 stars within this range, we extend it to ± 2 mag around the oMSTO. For Eri II, which is both the most populated and most distant of all galaxies in our sample, we restrict the fits to ± 0.75 mag around the oMSTO; this helps reduce errors from low-S/N sources at the faint end. We show an example set of Hess diagrams from the CMD modeling process for Hercules in Figure 8. The model provides an excellent match to the data, with few points discrepant at a level $> 3\sigma$.

Once the best-fit SFHs are in hand, we calculate the statistical uncertainties on them using a Hamiltonian Monte Carlo algorithm (S. Duane et al. 1987), as described in A. E. Dolphin (2013). We do not compute systematic uncertainties, which are designed to capture shortcomings of stellar evolution models (A. E. Dolphin 2012), as we are primarily interested in differences between the SFHs in a relative sense. We show all cumulative SFH fits with 68% confidence intervals in Figure 9.

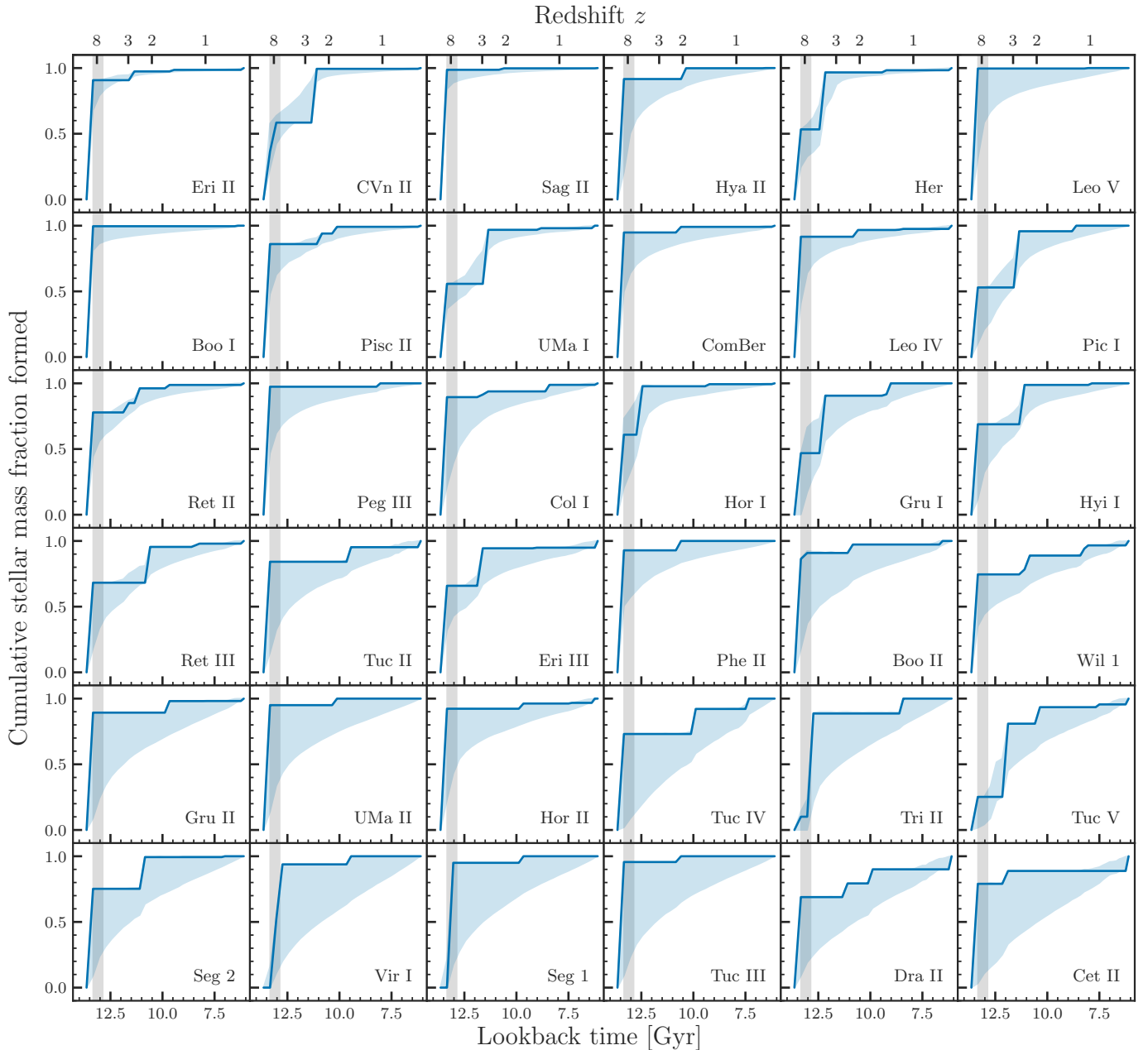


Figure 9. Best-fit SFHs for all UFDs (blue lines) with 68% confidence intervals (light blue shaded regions). The epoch of reionization is marked with the gray vertical bands (12.87 – 13.33 Gyr ago in Λ CDM; Planck Collaboration et al. 2020; M. Boylan-Kolchin & D. R. Weisz 2021). Uncertainties are from random errors only, and do not include systematic uncertainties on models or on galaxy parameters such as distance and reddening.

3.4. Quenching timescales

The epoch at which a galaxy ceases forming stars, or quenches, is an important quantity for understanding the physical processes that drive its lifetime evolution, such as feedback, environmental effects, and—in the case of UFDs—reionization. However, its interpretation from CMD-based SFH measurements is rarely straightforward. Often, a metric is adopted that describes the lookback time by which some fraction of the

total stellar mass has formed, denoted τ_q , where q is a percentage (e.g., D. R. Weisz et al. 2014a, 2015; E. D. Skillman et al. 2017).

While τ_{90} is the typical choice for more massive galaxies, UFDs are especially vulnerable to inflated estimates of late-time star formation from small numbers of spurious sources, such as unrejected foreground main sequence stars or blue stragglers, both of which can mimic younger stellar populations due to their CMD locations. We attribute the low levels of relatively recent star for-

mation ($\lesssim 10$ Gyr ago) found in Cet II, Dra II and Wil I to such spurious populations (see Figure 5, Figure 9, and Table 3). Each of these have several stars near the oMSTO that are slightly too blue to belong to the dominant population, such that they are interpreted by the SFH fitting software as younger populations; however, it is unclear if these stars are truly young, or if they are blue stragglers or non-members.

Therefore, we prefer the more conservative τ_{80} as our fiducial quenching time, following A. Savino et al. (2023) and K. B. W. McQuinn et al. (2024). Using this definition, we find an average quenching time of 12.48 ± 0.18 Gyr ago ($z = 4.6_{-0.5}^{+0.6}$ in Λ CDM), broadly consistent with previous studies (T. M. Brown et al. 2014; E. Sacchi et al. 2021) and with the end of the epoch of reionization in Λ CDM (Planck Collaboration et al. 2020; M. Boylan-Kolchin & D. R. Weisz 2021). (Note that this value includes Sag II; excluding it shifts the average lookback time to 12.45 Gyr.) We report all τ_{80} values in Table 3, and include τ_{50} and τ_{90} as well for completeness. In the remainder of the analysis, we present results for both τ_{80} and τ_{90} , but take τ_{80} as the fiducial quenching epoch. All reported τ values and their uncertainties are derived by interpolating the cumulative star formation histories shown in Figure 9; τ_{80} , for example, is the best-fit value (dark blue lines) at a cumulative stellar mass fraction of 0.8, and the upper and lower uncertainties are the limits of the 68% confidence window (light blue patches) at the same mass fraction.

4. DISCUSSION

4.1. Recommendations for robust MSTO fitting

Our SFHs vary greatly in precision, largely as a function of intrinsic luminosity and of total observed area relative to the galaxy profile. In Figure 10 we examine the 1σ width of the uncertainty on τ_{80} as a function of the effective V magnitude $M_{V\text{eff}}$ of the *HST* observations as defined in section 2, and of the number of stars within ± 1 magnitude of the oMSTO. The marker colors represent the signal-to-noise at the oMSTO ($M_{F606W} = 3.5$).

We find that a well-sampled stellar population—both in terms of the observational footprint and the galaxy’s total stellar mass itself—vastly outweighs photometric S/N for the purposes of achieving precise CMD-based SFHs, at least in the high-S/N limit of our data. Although Eri II has the lowest S/N at the oMSTO (~ 50), it is also by far the best populated; conversely, Dra II has the highest S/N—nearly 900—near the oMSTO, but simply has too few stars to meaningfully discriminate among isochrones.

Crucially, these results demonstrate that there is a lower bound on not only the effective luminosity for

which oMSTO fitting can reasonably be applied, but on the intrinsic luminosity of the galaxy as well, indicating a stellar mass threshold below which CMD fitting ceases to be effective as a means of SFH determination. Of course, this threshold is dependent on the acceptable uncertainties for a given science case. For the purposes of testing patchy reionization, we prefer uncertainties on τ_{80} below 500 Myr, so that an average of at least three galaxies can achieve an uncertainty less than half of the predicted ~ 500 -600 Myr time lag in quenching (R. Lunnan et al. 2012; T. Y. Li et al. 2014; D. Aubert et al. 2018; H. Zhu et al. 2019; H. Katz et al. 2020; P. Ocvirk et al. 2020; J. Kim et al. 2023). The faintest galaxy at which we reach this limit is Hyi I at $M_{V\text{eff}} = -2.5$; this corresponds to ~ 100 stars within ± 1 mag of the oMSTO, consistent with the recommendation of T. M. Brown et al. (2014). More lax uncertainty thresholds (e.g., 1 Gyr) may be acceptable for the purpose of measuring ensemble quenching timescales.

For the galaxies in our sample, observations over a larger area (e.g., with the upcoming Nancy Grace Roman Space Telescope) would be most beneficial in the cases of UMa II, Tuc IV, and Gru II, all of which have $M_V \leq -3.5$ but $f_* \leq 0.1$ ($M_{V\text{eff}} \geq -1.9$). Improving the S/N at the oMSTO, despite its generally marginal effects at both the well- and sparsely-populated extremes, would be most useful in Col I, Leo V, Peg III, and Pisc II, which have $S/N_{\text{MSTO}} < 100$. These are otherwise well-sampled populations for which star-galaxy separation near the turnoff is poorest, which may have the effect of biasing the SFHs or inflating their uncertainties (see Figure 4 and Figure 9).

Additional potential avenues for improvement in future studies include: a) robust membership information at fainter magnitudes, via deeper proper motion data (e.g., with future *Gaia* data releases or Vera C. Rubin observations) and/or velocities (e.g. with ELTs); and b) use of a filter pair with a broader color baseline. We stress that the F606W–F814W filter combination is sub-optimal for SFH fitting due to its narrow color separation, where sensitivity to metallicity variations is minimal. The F475W–F814W combination on ACS/WFC and WFC3/UVIS offers much greater leverage on color and thus metallicity (as demonstrated by A. Savino et al. 2025), but at greater observational cost. The F475W–F814W combination is only available in the *HST* archive for 17 of the galaxies in this study as of this writing. This is less than half of our sample, and the majority of the F475W observations are much shallower than the F606W, targeting the red giant branch rather than the MSTO.

Table 3. Stellar mass formation lookback times

Galaxy	Kinematic group	τ_{50} [Gyr]	τ_{80} [Gyr]	τ_{90} [Gyr]
Boo I	Long-term MW	$13.49^{+0.00}_{-0.04}$	$13.40^{+0.00}_{-0.06}$	$13.37^{+0.00}_{-1.03}$
Boo II	Long-term MW	$13.47^{+0.00}_{-0.99}$	$13.36^{+0.00}_{-3.92}$	$13.09^{+0.08}_{-5.56}$
CVn II	First infall	$13.15^{+0.23}_{-0.44}$	$11.21^{+0.63}_{-0.04}$	$11.15^{+0.23}_{-0.07}$
Cet II	Long-term MW	$13.45^{+0.00}_{-2.96}$	$12.13^{+0.02}_{-4.66}$	$6.22^{+1.77}_{-0.00}$
Col I	Long-term MW	$13.47^{+0.00}_{-0.70}$	$13.37^{+0.00}_{-2.64}$	$11.82^{+0.00}_{-3.33}$
ComBer	Long-term MW	$13.48^{+0.00}_{-0.15}$	$13.38^{+0.00}_{-1.57}$	$13.35^{+0.00}_{-3.69}$
Dra II	Long-term MW	$13.42^{+0.00}_{-2.65}$	$10.10^{+0.00}_{-2.43}$	$9.89^{+0.00}_{-3.30}$
Eri II	First infall	$13.48^{+0.00}_{-0.06}$	$13.37^{+0.00}_{-0.40}$	$13.34^{+0.00}_{-1.23}$
Eri III	Long-term MW	$13.41^{+0.00}_{-1.01}$	$11.75^{+0.05}_{-1.78}$	$11.66^{+0.02}_{-4.19}$
Gru I	Long-term MW	$12.43^{+0.86}_{-0.16}$	$12.23^{+0.11}_{-2.34}$	$12.17^{+0.01}_{-3.75}$
Gru II	Long-term MW	$13.47^{+0.00}_{-1.58}$	$13.37^{+0.00}_{-4.66}$	$9.87^{+0.00}_{-2.55}$
Her	Long-term MW	$13.36^{+0.00}_{-0.99}$	$12.27^{+0.09}_{-0.46}$	$12.21^{+0.04}_{-0.80}$
Hor I	LMC	$13.39^{+0.04}_{-0.73}$	$12.59^{+0.45}_{-0.63}$	$12.51^{+0.16}_{-2.27}$
Hor II	Long-term MW	$13.48^{+0.00}_{-0.63}$	$13.38^{+0.00}_{-3.53}$	$13.34^{+0.00}_{-5.56}$
Hya II	First infall	$13.48^{+0.00}_{-0.44}$	$13.38^{+0.00}_{-2.08}$	$13.34^{+0.00}_{-3.67}$
Hyi I	LMC	$13.42^{+0.00}_{-1.16}$	$11.25^{+0.26}_{-0.50}$	$11.17^{+0.07}_{-2.14}$
Leo IV	First infall	$13.48^{+0.00}_{-0.26}$	$13.38^{+0.00}_{-1.44}$	$13.34^{+0.00}_{-3.50}$
Leo V	Long-term MW	$13.49^{+0.00}_{-0.36}$	$13.40^{+0.00}_{-1.82}$	$13.37^{+0.00}_{-4.13}$
Peg III	Long-term MW	$13.49^{+0.00}_{-0.22}$	$13.39^{+0.00}_{-1.63}$	$13.36^{+0.00}_{-3.76}$
Phe II	LMC	$13.48^{+0.00}_{-0.14}$	$13.38^{+0.00}_{-2.30}$	$13.35^{+0.00}_{-4.32}$
Pic I	Long-term MW	$13.35^{+0.00}_{-1.57}$	$11.45^{+0.11}_{-0.96}$	$11.39^{+0.04}_{-2.65}$
Pisc II	Long-term MW	$13.47^{+0.00}_{-0.17}$	$13.36^{+0.00}_{-1.72}$	$10.97^{+0.39}_{-0.78}$
Ret II	LMC	$13.45^{+0.00}_{-0.26}$	$11.80^{+0.50}_{-0.48}$	$11.24^{+0.07}_{-1.29}$
Ret III	Long-term MW	$13.42^{+0.00}_{-1.19}$	$10.73^{+0.41}_{-0.74}$	$10.64^{+0.04}_{-2.44}$
Sag II	Long-term MW	$13.49^{+0.00}_{-0.03}$	$13.39^{+0.00}_{-0.04}$	$13.36^{+0.00}_{-0.52}$
Seg 1	Long-term MW	$13.18^{+0.04}_{-1.56}$	$13.08^{+0.01}_{-4.36}$	$13.05^{+0.00}_{-5.69}$
Seg 2	Long-term MW	$13.44^{+0.00}_{-1.87}$	$11.04^{+0.01}_{-2.16}$	$10.94^{+0.01}_{-3.48}$
Tri II	Long-term MW	$12.88^{+0.03}_{-1.44}$	$12.77^{+0.01}_{-4.36}$	$8.59^{+0.02}_{-1.35}$
Tuc II	Long-term MW	$13.46^{+0.00}_{-1.12}$	$13.35^{+0.00}_{-4.24}$	$9.55^{+0.01}_{-2.16}$
Tuc III	Long-term MW	$13.48^{+0.00}_{-1.67}$	$13.39^{+0.00}_{-4.52}$	$13.35^{+0.00}_{-5.90}$
Tuc IV	Long-term MW	$13.43^{+0.00}_{-3.12}$	$10.03^{+0.02}_{-2.34}$	$9.91^{+0.00}_{-2.78}$
Tuc V	Long-term MW	$12.04^{+0.43}_{-0.48}$	$11.89^{+0.00}_{-3.42}$	$10.42^{+0.00}_{-3.43}$
UMa I	First infall	$13.37^{+0.00}_{-1.05}$	$11.46^{+0.19}_{-0.09}$	$11.39^{+0.07}_{-0.96}$
UMa II	Long-term MW	$13.48^{+0.00}_{-1.03}$	$13.39^{+0.00}_{-4.04}$	$13.35^{+0.00}_{-5.66}$
Vir I	Long-term MW	$13.05^{+0.01}_{-2.13}$	$12.83^{+0.00}_{-4.74}$	$12.76^{+0.00}_{-5.71}$
Wil 1	Long-term MW	$13.44^{+0.00}_{-0.81}$	$11.05^{+0.00}_{-2.26}$	$8.37^{+0.08}_{-0.93}$

4.2. Comparison with literature

In this section, we undertake a comparison between the 14 MW UFDs in the literature that have SFHs and those presented in this paper. Two papers, [T. M. Brown et al. \(2014\)](#) and [E. Sacchi et al. \(2021\)](#), contain virtually all literature UFD SFHs. Accordingly, we focus most of our comparisons on these two systematic studies.

[T. M. Brown et al. \(2014\)](#) reported SFHs of six UFDs (Boo I, CVn II, Com Ber, Her, Leo IV, and UMa I). They used custom Victoria-Regina isochrones ([D. A. Vandenberg et al. 2014a,b](#)) along with spectroscopic

metallicity distribution functions of red giants measured from Keck spectra, and theoretical [O/Fe] abundances varying as a function of [Fe/H]. SFHs were measured as two-burst models, with absolute ages set relative to a fiducial SSP model of M92. Distances and foreground reddenings to each galaxy were included as free parameters in the fits.

[E. Sacchi et al. \(2021\)](#) presented SFHs of seven UFDs: Hor I, Hya II, Phe II, Ret II, Sag II, Tri II, and Tuc II. They use the SFERA software ([M. Cignoni et al. 2015](#)) with two sets of isochrones: Victoria-Regina with $[\alpha/\text{Fe}]$

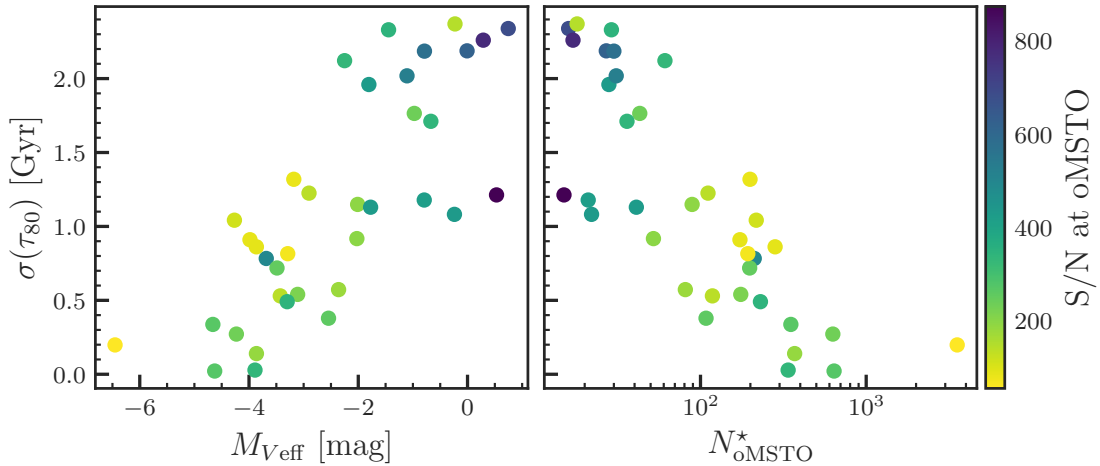


Figure 10. Error on τ_{80} (half the width of the 68% confidence interval) against the effective V magnitude of the *HST* observations, $M_{V\text{eff}} = M_V - 2.5 \log_{10}(f_*)$ (left), and the number of stars within ± 1 mag of the F606W oMSTO (right; $2.5 < M_{F606W} < 4.5$), colored by S/N at the F606W oMSTO. From these we infer $M_{V\text{eff}} \leq -2.5$ or 100 oMSTO stars as the limits for which one can derive precise SFHs, with S/N as a minor secondary factor.

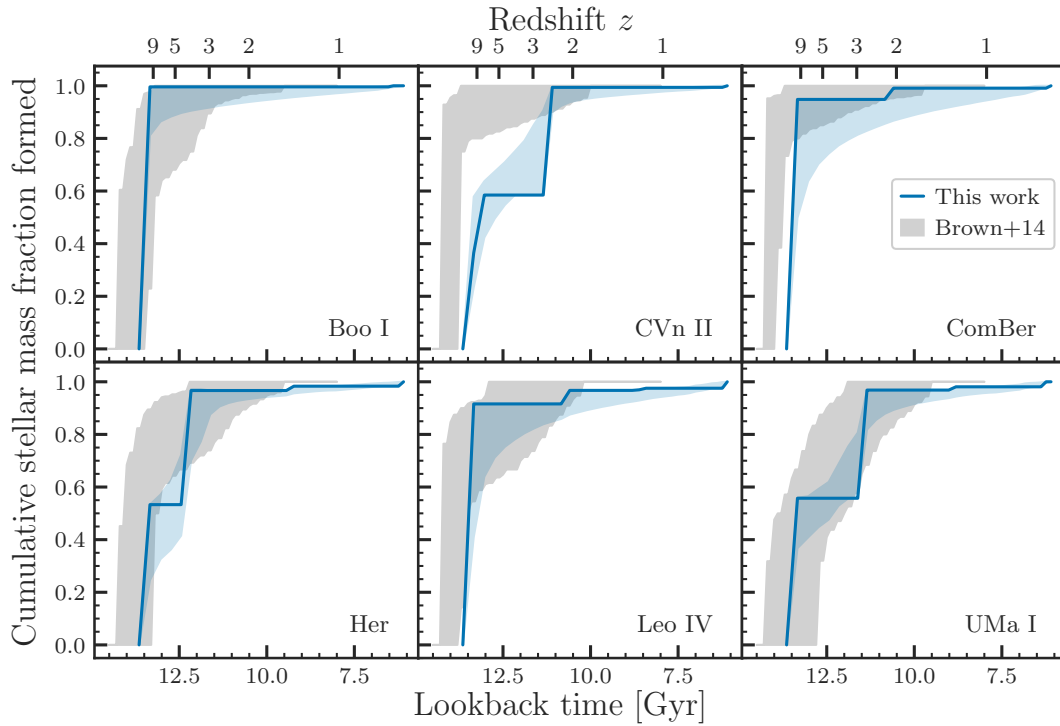


Figure 11. Comparison of the SFHs derived in this work (blue) with the SFHs reported by T. M. Brown et al. (2014, gray patches). We find excellent agreement in most cases, with only minor exceptions.

= +0.4 (D. A. VandenBerg et al. 2014a,b), and scaled-solar MIST (A. Dotter 2016).

As shown in Figure 11, our SFHs are generally in good agreement with those reported by T. M. Brown et al. (2014), modulo respective choices of oldest age limit (14.1 vs. 13.7 Gyr). Nearly all galaxies exhibit similar qualitative SFH shapes and overlapping uncertainties.

Only CVn II shows any noticeable discrepancy above the 1σ level at lookback times greater than ~ 12 Gyr. Further, our SFH for CVn II has a quenching time > 10 Gyr ago, like T. M. Brown et al. (2014). This is older than the ~ 8 Gyr quenching epoch reported by D. R. Weisz et al. (2014b), which used lower S/N HST/WFPC2 data

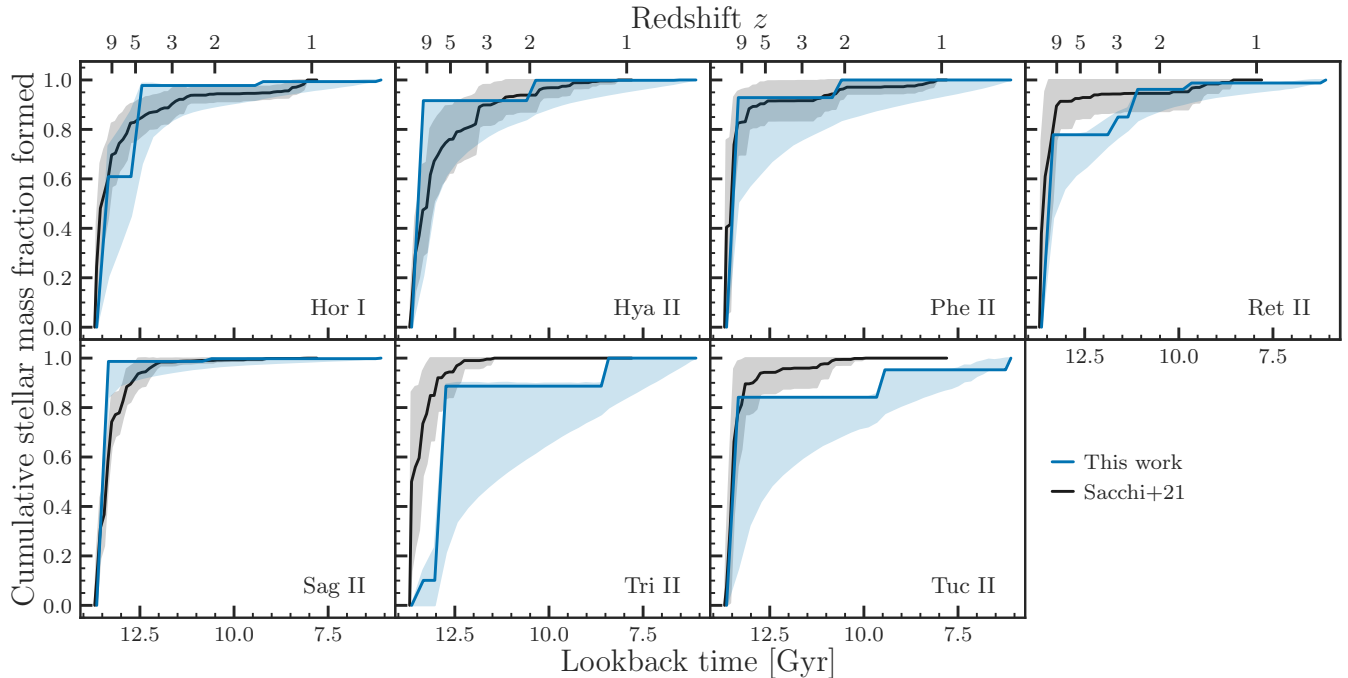


Figure 12. As Figure 11, with the SFHs reported by E. Sacchi et al. (2021) as black lines. Again, we see generally excellent agreement with some exceptions. The two galaxies with the strongest disagreement, Tri II and Tuc II, have large error bars in our fits.

and a different distance/extinction combination to measure the SFH.

We note that our distance modulus to Hercules is ~ 0.3 mag closer than that of T. M. Brown et al. (2014) (20.63 vs. 20.92), and Leo IV is 0.25 mag closer (20.87 vs. 21.12), but the rest are within ± 0.1 mag of each other. The extinctions show small offsets, with ours systematically lower than those of T. M. Brown et al. (2014) by ~ 0.05 -0.1 mag.

The comparison with E. Sacchi et al. (2021) is for the most part favorable, with minor exceptions. As illustrated in Figure 12, Hor I, Hya II, Phe II, and Sag II all have overlapping uncertainties at more or less all ages. For Ret II we find evidence of a slightly younger secondary population ($\sim 20\%$ by mass, formed between 12.5-11 Gyr ago) that is absent in E. Sacchi et al. (2021). We find Tri II and Tuc II to be somewhat younger than E. Sacchi et al. (2021), but the large error bars on our results for these two galaxies indicate that these differences should not be over-interpreted.

There is also generally good agreement between our SFHs and the handful of single galaxy SFH papers in the literature. For example, J. D. Simon et al. (2023) measure the SFH of Ret II using the same 12 HST fields as our analysis (compared to the single field of Ret II analyzed by E. Sacchi et al. 2021). Our SFH of Ret II is consistent with that of J. D. Simon et al. (2023), who

also find that up to 20% of the stellar mass formed in a secondary burst ~ 11 Gyr ago.

There is modest disagreement in the literature over the SFH of Eri II. Our SFH shows that Eri II formed 90% of its stellar mass prior to ~ 13 Gyr ago and the remaining 10% between 12.5 and ~ 9 Gyr ago. J. D. Simon et al. (2021) analyze the same deep HST data and find that 80% of the star formation occurred by ~ 13 Gyr ago, with the remainder concluding by no later than ~ 10 Gyr ago. Using multiple deep HST datasets, C. Gallart et al. (2021) find that star formation in Eri II likely entirely concluded by ~ 13 Gyr, and that the low-level star formation, $\sim 20\%$ of the total stellar mass, that extends to ~ 9 Gyr ago is consistent with zero star formation at these younger ages. Finally, D. R. Weisz et al. (2023) use archival HST imaging to measure the SFH of Eri II, and its globular cluster, and find similar solutions: $\sim 70\%$ of its stellar mass formed by ~ 13 Gyr ago and 20% formed 11-12 Gyr ago. The main differences among these solutions appear to the significance attributed to any star formation younger than ~ 13 Gyr. C. Gallart et al. (2021) and J. D. Simon et al. (2021) both conclude that the younger episodes of star formation are of low significance, whereas D. R. Weisz et al. (2023) and the present paper suggest the younger star formation is significant at least at the 68% confidence level. The differences in analysis techniques,

adopted oldest ages, and varying uncertainty computations makes it challenging to directly compare these results. However, we emphasize that the studies are generally telling the same story: Eri II is a pre-reionization fossil with marginal evidence of extended star formation to no more than ~ 11 Gyr ago.

As part of developing a new SFH fitting code, C. T. Garling et al. (2024) measure the SFH of Hor I using the same HST imaging as in this paper. They report a SFH that is marginally younger than that of E. Sacchi et al. (2021), which is similar to our SFH of this galaxy.

4.3. Environmental quenching differences

In patchy reionization scenarios, the progenitors of MW- and M31-sized galaxies, which were dispersed throughout the volume of the proto-Local Group, as well as progenitors of their present day satellites, may have experienced reionization at different times. The timing and amplitude of reionization are thought to be functions of local galaxy density, as well as internal factors such as escape fraction of ionizing photons. Because of their low halo masses, star formation in UFDs at the time of reionization is thought to be particularly sensitive to the impacts of reionization. Indeed, several simulations suggest that patchy reionization can lead to spreads in the times at which reionization impacts (i.e., quenches) the lowest-mass galaxies by up to 400-600 Myr depending on their environment at the time of reionization (e.g., C. M. Simpson et al. 2013; D. Aubert et al. 2018; J. Kim et al. 2023). These time differences are typically measured across many progenitor halos over volumes thought to be comparable to the ancient LG environment. However, the surviving satellites of a single MW-mass host halo may still bear imprints of patchy reionization, depending on their proximity to the nearest massive halo during reionization and the spatial scales over which massive halos drive early reionization (e.g., A. R. Wetzel et al. 2015; Y. Zhao et al. 2025).

We consider whether such signatures are present in our data by comparing the SFHs of UFDs that have different kinematic memberships (e.g., MW satellites vs. LMC satellites vs. first-infall) as determined by the best-available orbital histories to date. These different groups may proxy different environmental conditions in the early Universe. Though the exact locations of UFDs at the time of reionization are unknown, the orbital histories provide the best available empirical constraints on their likely locations (e.g., higher vs lower density regions) in the early Universe. We discuss caveats implicit in this assumption below.

In Figure 13 we show combined SFHs of all 36 galaxies (upper panel) and the 17 galaxies with $M_{V\text{eff}} \leq -2.5$

(see Figure 10), aggregated by kinematic group. We exclude Sag II from the latter due to its status as a likely globular cluster (N. Longeard et al. 2021). We assign galaxies to kinematic groups based on recent work on their orbital histories (T. K. Fritz et al. 2018; N. Kallivayalil et al. 2018; S. P. Fillingham et al. 2019; E. Patel et al. 2020; A. B. Pace et al. 2022). We consider Hor I, Hyi I, Phe II, and Ret II to be LMC satellites (either long-term or recently captured; E. Patel et al. 2020), and CVn II, Eri II, Hya II, Leo IV, and UMa I to be on their first infall into the MW halo. We consider the rest of the sample to be long-term MW satellites by default. Of the galaxies with $M_{V\text{eff}} \leq -2.5$, this includes Boo I, Col I, ComBer, Gru I, Her, Leo V, Peg III, Pic I, and Pisc II.

We compute the average SFHs of each kinematic group in two ways. First, we take a simple, unweighted average of the best-fit lookback times as a function of the mass fraction formed. Second, we compute the weighted average of the same quantities. For the weighting, we take the standard deviation of the lookback time at mass fraction X , $\sigma(\tau_X)$, to be half the width of the 68% confidence interval, and weight by the inverse variance $\sigma(\tau_X)^{-2}$. All reported uncertainties on the averaged SFHs are the standard error on the mean. We report all average τ_{80} and τ_{90} values and uncertainties, and the differences between kinematic groups, in Table 4.

In the unweighted case (top panels of Figure 13), we find marginal signal of a delay by comparing population averages. The main notable difference is a delay between the long-term MW and LMC τ_{80} in the culled sample ($\Delta\tau_{80} = 1.04 \pm 0.46$) at the level of $\sim 2\sigma$. $\Delta\tau_{90}$ shows no significant difference. A second difference is a modest delay in τ_{90} of long-term MW satellites vs. the first infall group in the unculted sample ($\Delta\tau_{80} = -1.02 \pm 0.63$), which is of low statistical significance.

One challenge in interpreting the unweighted averages is that the sample is dominated by the lowest-mass systems, which have the largest uncertainties in their SFHs. The amplitude of the SFH uncertainties on these faint systems is larger than the \sqrt{N} gain realized by increasing the sample size. The result is that the addition of faint galaxies to the unweighted averaging does not result in better constraints on the population mean. Accordingly, we consider a weighted-averaging scheme to mitigate these effects.

In the weighted scenario, we find larger quenching delays of $\Delta\tau_{80} = 1.33$ -1.65 Gyr between the culled long-term MW and both first-infall and LMC groups, at up to 5σ significance. A major factor for this change is a result of Boo I dominating the long-term MW group due to its

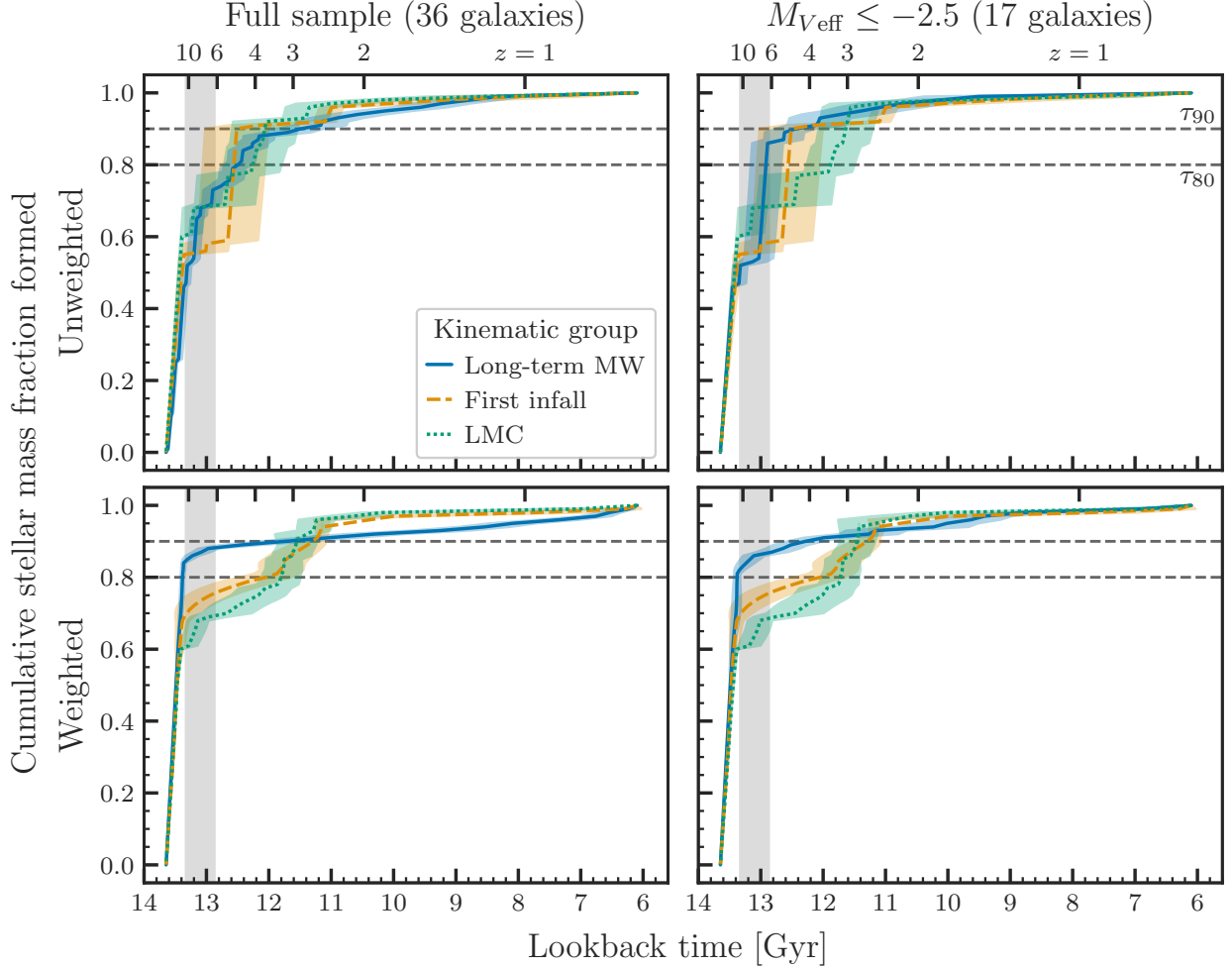


Figure 13. Average SFHs by kinematic group for our full galaxy sample (left column) and galaxies with $M_{V,\text{eff}}$ less than -2.5 (right column), computed as simple averages (upper row) and inverse variance-weighted averages (lower row). We see significant differences in τ_{80} and τ_{90} (black dashed lines) between the long-term MW sample and the other two kinematic groups only in the weighted averages, whereas the unweighted averages show largely marginal differences.

Table 4. Average τ_{80} and τ_{90} values and differences by kinematic group

Group	N	τ_{80} [Gyr]	τ_{90} [Gyr]	$\Delta\tau_{80}$, MW - X	$\Delta\tau_{90}$, MW - X
Unweighted					
Long-term MW	9 (27)	12.92 ± 0.25 (12.49 ± 0.21)	12.44 ± 0.32 (11.49 ± 0.37)	—	—
First infall	5 (5)	12.56 ± 0.50 (12.56 ± 0.56)	12.51 ± 0.51 (12.51 ± 0.51)	0.36 ± 0.56 (-0.07 ± 0.54)	-0.07 ± 0.60 (-1.02 ± 0.63)
LMC	3 (4)	11.88 ± 0.39 (12.26 ± 0.46)	11.64 ± 0.44 (12.06 ± 0.53)	1.04 ± 0.46 (0.23 ± 0.51)	0.80 ± 0.54 (-0.57 ± 0.65)
Weighted					
Long-term MW	9 (27)	13.38 ± 0.05 (13.38 ± 0.03)	12.28 ± 0.29 (11.73 ± 0.39)	—	—
First infall	5 (5)	12.05 ± 0.41 (12.05 ± 0.41)	11.30 ± 0.23 (11.30 ± 0.23)	1.33 ± 0.41 (1.33 ± 0.41)	0.98 ± 0.37 (0.43 ± 0.45)
LMC	3 (4)	11.73 ± 0.31 (11.81 ± 0.32)	11.45 ± 0.29 (11.55 ± 0.33)	1.65 ± 0.31 (1.57 ± 0.32)	0.83 ± 0.41 (0.18 ± 0.51)

NOTE—We present values for the culled galaxy sample first, and for the full sample in parentheses after. The culled sample is restricted to galaxies with $M_{V,\text{eff}} \leq -2.5$, and excludes Sag II, as in the second column of Figure 13.

low uncertainties and uniformly ancient SFH. We also note that the weighted τ_{80} and τ_{90} averages for the first-infall and LMC groups are consistently younger than the unweighted values. The $\Delta\tau_{90}$ values between the long-term MW and LMC groups in the culled sample are the most consistent across the weighted and unweighted averages (0.80 ± 0.54 and 0.83 ± 0.41 Gyr respectively). We find a slightly larger delay than that reported by E. Sacchi et al. (2021), who measured a ~ 600 Myr delay in τ_{90} for the LMC group compared to the long-term MW group using the same error-weighted averaging approach.

While we find a modest signal in the SFHs that could be attributed to patchy reionization, there are several important caveats and considerations. First, the orbital histories are not well-constrained back to the reionization-era. We have assumed that the kinematic group traces different ancient environments. Some simulations suggest that all present-day UFDs were located in comparably low-density regions around the proto-Local Group (e.g., M. K. Rodriguez Wimberly et al. 2019), whereas others expect more environmental variations (e.g., D. Aubert et al. 2018; J. Kim et al. 2023). We cannot resolve this tension in the present study and only note it as a caveat. Second, the averaging methods produce different results. The signal of SFH differences in our weighted average matches or exceeds that reported by E. Sacchi et al. (2021). But, results from our unweighted average are more modest. A fair comparison with theory requires that both simulation and observations studies adopt the same population-wide metrics. Importantly, we have included all data necessary for an interested reader to conduct their own population-level averages. Finally, some of the variation in quenching timescales is likely driven by processes beyond reionization alone. The suppression of UFD star formation by reionization is modulated by supernova feedback and subsequent gas accretion, where galaxies that lost their gas supply before reionization could not restart star formation, while those that retained some gas were able to sustain star formation post-reionization (e.g., J. S. Bullock et al. 2000; M. Ricotti & N. Y. Gnedin 2005; M. Jeon et al. 2017). Although the star-forming lifetimes of many of these galaxies are far longer than the timescales on which Type II SNe occur, several factors play a role in determining the extent to which a given supernova contributes to the suppression of star formation. These include the location of the supernova with respect to the bulk of the galaxy gas content, the mass of the dark matter halo, and the energetics of the supernova itself (e.g., D. Webster et al. 2015; J. Bland-Hawthorn et al. 2015; M. Jeon et al. 2017). These effects, combined with

hierarchical assembly processes, may explain the diversity in observed UFD SFHs and highlight the need to account for spatially inhomogeneous reionization when interpreting MW satellite populations.

Despite these caveats, we can place an upper limit on a measureable signal ($\lesssim 800$ Myr) which is consistent with current predictions from simulations of patchy reionization in the local Universe. The main obstacle to improving the empirical constraints are the lack of UFDs for which very secure SFHs can be measured and the noise that is introduced by the inherently stochastic SFHs of very sparsely populated systems.

5. CONCLUSIONS

We have measured deep, uniform *HST* photometry and SFHs of 36 UFDs based on CMD fitting. We recommend observations with $M_{V\text{eff}} \leq -2.5$ ($N_{\text{oMSTO}}^* \geq 100$) and $S/N \geq 100$ at the oMSTO for a high-quality SFH fit. Lower S/N (~ 50 - 100) may still be adequate for well-sampled populations ($M_{V\text{eff}} \lesssim 5$), but robust star-galaxy separation at the oMSTO is important in more marginal cases.

As in prior work, we find moderate evidence of a delay in quenching of star formation in LMC satellites and first-infall galaxies relative to long-term Galactic satellites, although its duration and statistical significance are subject to a number of confounding factors. We find a global average quenching time of 12.48 ± 0.18 Gyr ago, consistent with reionization-driven quenching scenarios, and place an upper limit on the quenching time delay of ~ 800 Myr, at 2σ significance.

In the future, samples of truly isolated field UFDs as well as satellite systems outside the Local Group will provide critical benchmarks for disentangling the effects of patchy reionization vs. other environmental and internal factors (e.g., tidal and ram pressure stripping, supernova feedback).

ACKNOWLEDGMENTS

We thank Tom Brown for sharing his star formation history fit results with us. Support for this work was provided by NASA through grants GO-16293 and AR-17026 from the Space Telescope Science Institute, which is operated by AURA, Inc., under NASA contract NAS5-26555. The Flatiron Institute is funded by the Simons Foundation. This research made use of hips2fits,²⁰ a service provided by CDS. This work has made use of data from the European Space Agency (ESA)

²⁰ <https://alasky.cds.unistra.fr/hips-image-services/hips2fits>

mission *Gaia* (<https://www.cosmos.esa.int/gaia>), processed by the *Gaia* Data Processing and Analysis Consortium (DPAC, <https://www.cosmos.esa.int/web/gaia/dpac/consortium>). Funding for the DPAC has been provided by national institutions, in particular the institutions participating in the *Gaia* Multilateral Agreement. This research has made use of NASA's Astrophysics Data System. This research has made use of the VizieR catalogue access tool, CDS, Strasbourg, France (DOI: 10.26093/cds/vizieR). The original description of the VizieR service was published in F. Ochsenbein et al. (2000). This research uses services or data provided by the Astro Data Lab, which is part of the Community Science and Data Center (CSDC) Program of NSF NOIRLab. NOIRLab is operated by the Association of Universities for Research in Astronomy (AURA), Inc. under a cooperative agreement with the U.S. National Science Foundation. The Pan-STARRS1 Surveys (PS1) and the PS1 public science archive have been made possible through contributions by the Institute for Astronomy, the University of Hawaii, the Pan-STARRS Project Office, the Max-Planck Society and its participating institutes, the Max Planck Institute for Astronomy, Heidelberg and the Max Planck Institute for Extraterrestrial Physics, Garching, The Johns Hopkins University, Durham University, the University of Edinburgh, the Queen's University Belfast, the Harvard-Smithsonian Center for Astrophysics, the Las Cumbres Observatory Global Telescope Network Incorporated, the National Central University of Tai-

wan, the Space Telescope Science Institute, the National Aeronautics and Space Administration under Grant No. NNX08AR22G issued through the Planetary Science Division of the NASA Science Mission Directorate, the National Science Foundation Grant No. AST-1238877, the University of Maryland, Eotvos Lorand University (ELTE), the Los Alamos National Laboratory, and the Gordon and Betty Moore Foundation.

Facilities: HST (ACS). All the data presented in this paper were obtained from the Mikulski Archive for Space Telescopes (MAST) at the Space Telescope Science Institute. The specific observations analyzed can be accessed via DOI: 10.17909/06qe-m148. The HLSP products related to this paper can be accessed via DOI: 10.17909/b8yw-wv58.

Software: Astropy v6.0.1 (Astropy Collaboration et al. 2013, 2018, 2022), Astroquery v0.4.7 (A. Ginsburg et al. 2017, 2019, 2021), DOLPHOT v2.0 (A. E. Dolphin 2000; A. Dolphin 2016), Drizzlepac v3.6.1 (STSCI Development Team 2012; W. J. Hack et al. 2013; R. J. Avila et al. 2015), `hst1pass` v2024.05.29 (J. Anderson 2022), MATCH (A. E. Dolphin 2002), Matplotlib v3.9.2 (J. D. Hunter 2007; The Matplotlib Development Team 2023), NumPy v1.25.2 (S. van der Walt et al. 2011; C. R. Harris et al. 2020), pandas v2.2.3 (W. McKinney 2010; The pandas development Team 2023), seaborn v0.13.2 (M. Waskom et al. 2020, 2023; M. Waskom 2021), SciPy v1.10.0 (P. Virtanen et al. 2020), Vaex v4.17.0 (M. A. Breddels & J. Veljanoski 2018a,b)

APPENDIX

A. PHOTOMETRY PRODUCT DESCRIPTIONS

Here we describe the contents of the DOLPHOT full-stack (source-level) photometry catalogs included in this data release. For in-depth descriptions of the DOLPHOT routines and outputs, please see A. E. Dolphin (2000) and the DOLPHOT user manual.²¹ Table 5 describes the columns of the DOLPHOT catalogs, which are provided in FITS tabular format.

REFERENCES

- Anderson, J. 2022,, Instrument Science Report WFC3 2022-5, 55 pages
- Anderson, J., & King, I. R. 2000, PASP, 112, 1360, doi: 10.1086/316632
- Anderson, J., & King, I. R. 2006,, Instrument Science Report ACS 2006-01
- Astropy Collaboration, Robitaille, T. P., Tollerud, E. J., et al. 2013, A&A, 558, A33, doi: 10.1051/0004-6361/201322068
- Astropy Collaboration, Price-Whelan, A. M., Sipőcz, B. M., et al. 2018, AJ, 156, 123, doi: 10.3847/1538-3881/aabc4f
- Astropy Collaboration, Price-Whelan, A. M., Lim, P. L., et al. 2022, ApJ, 935, 167, doi: 10.3847/1538-4357/ac7c74
- Aubert, D., Deparis, N., Ocvirk, P., et al. 2018, ApJL, 856, L22, doi: 10.3847/2041-8213/aab14d

²¹ <http://americano.dolphinim.com/dolphot/dolphot.pdf>

Table 5. Description of columns in the DOLPHOT photometric catalogs.

Column	Type	Unit	Description
ID	str		Unique source identifier within the field
RA	float32	deg	Right Ascension (ICRS)
DEC	float32	deg	Declination (ICRS)
X	float32	pix	X position in reference image (origin=0.5)
Y	float32	pix	Y position in reference image (origin=0.5)
OBJTYPE	uint8		Object type (1=bright star, 2=faint star)
For each filter ^a			
<i>Filter_COUNT</i>	float32	e ⁻	Total source counts, combined over all images in <i>Filter</i>
<i>Filter_SKY</i>	float32	e ⁻	Total sky level around source, combined over all images in <i>Filter</i>
<i>Filter_VEGA</i>	float32	mag	Vega ^b magnitude, combined over all images in <i>Filter</i>
<i>Filter_ERR</i>	float32	mag	Uncertainty on magnitude, combined over all images in <i>Filter</i>
<i>Filter_CHI</i>	float32		χ of the PSF fit, combined over all images in <i>Filter</i>
<i>Filter_SNR</i>	float32		Signal-to-noise ratio of the PSF fit, combined over all images in <i>Filter</i>
<i>Filter_SHARP</i>	float32		Sharpness of the PSF fit, combined over all images in <i>Filter</i>
<i>Filter_ROUND</i>	float32		Roundness of the PSF fit, combined over all images in <i>Filter</i>
<i>Filter_CROWD</i>	float32	mag	Crowding of the PSF fit, combined over all images in <i>Filter</i>
<i>Filter_FLAG</i>	uint8		Quality flag of the PSF fit, combined over all images in <i>Filter</i> (≤ 3 recommended)
<i>Filter_GST</i>	bool		Does the object pass the GST criteria in this filter?
For each image ^b			
<i>Image_COUNT</i>	float32	e ⁻	Source counts in <i>Image</i>
<i>Image_SKY</i>	float32	e ⁻	Sky level around source in <i>Image</i>
<i>Image_VEGA</i>	float32	mag	Vega magnitude of the PSF fit in <i>Image</i>
<i>Image_ERR</i>	float32	mag	Uncertainty on magnitude of the PSF fit in <i>Image</i>
<i>Image_CHI</i>	float32		χ of the PSF fit in <i>Image</i>
<i>Image_SNR</i>	float32		Signal-to-noise ratio of the PSF fit in <i>Image</i>
<i>Image_SHARP</i>	float32		Sharpness of the PSF fit in <i>Image</i>
<i>Image_ROUND</i>	float32		Roundness of the PSF fit in <i>Image</i>
<i>Image_CROWD</i>	float32	mag	Crowding of the PSF fit in <i>Image</i>
<i>Image_FLAG</i>	uint8		Quality flag of the PSF fit in <i>Image</i>

^a Filters are named as *camera_filter*, for example ACS_F814W.

^b Zeropoints are based on the CALSPEC Vega spectrum `alpha_lyr_stis.008.fits`.

^c Images are named as follows: `ippssoot_filter_sfx_chip#`, for example `jbpb02v9q.f814w_flg_chip1`. The `ippssoot` and `sfx` naming conventions are described further in the HST user documentation: <https://hst-docs.stsci.edu/hstdhb/2-hst-file-names/2-1-file-name-format>

- Avila, R. J., Hack, W., Cara, M., et al. 2015, in Astronomical Society of the Pacific Conference Series, Vol. 495, Astronomical Data Analysis Software and Systems XXIV (ADASS XXIV), ed. A. R. Taylor & E. Rosolowsky, 281, doi: [10.48550/arXiv.1411.5605](https://arxiv.org/abs/1411.5605)
- Bajaj, V. 2017,, Instrument Science Report WFC3 2017-19, 4 pages
- Bajaj, V., & Anderson, J. 2020, in American Astronomical Society Meeting Abstracts, Vol. 235, American Astronomical Society Meeting Abstracts #235, 109.07
- Battaglia, G., Taibi, S., Thomas, G. F., & Fritz, T. K. 2022, A&A, 657, A54, doi: [10.1051/0004-6361/202141528](https://doi.org/10.1051/0004-6361/202141528)
- Bechtol, K., Drlica-Wagner, A., Balbinot, E., et al. 2015, ApJ, 807, 50, doi: [10.1088/0004-637X/807/1/50](https://doi.org/10.1088/0004-637X/807/1/50)
- Becker, G. D., Bolton, J. S., Madau, P., et al. 2015, MNRAS, 447, 3402, doi: [10.1093/mnras/stu2646](https://doi.org/10.1093/mnras/stu2646)
- Benson, A. J., Frenk, C. S., Baugh, C. M., Cole, S., & Lacey, C. G. 2003, MNRAS, 343, 679, doi: [10.1046/j.1365-8711.2003.06709.x](https://doi.org/10.1046/j.1365-8711.2003.06709.x)
- Benson, A. J., Frenk, C. S., Lacey, C. G., Baugh, C. M., & Cole, S. 2002, MNRAS, 333, 177, doi: [10.1046/j.1365-8711.2002.05388.x](https://doi.org/10.1046/j.1365-8711.2002.05388.x)
- Besla, G., Kallivayalil, N., Hernquist, L., et al. 2007, ApJ, 668, 949, doi: [10.1086/521385](https://doi.org/10.1086/521385)

- Bland-Hawthorn, J., Sutherland, R., & Webster, D. 2015, *ApJ*, 807, 154, doi: [10.1088/0004-637X/807/2/154](https://doi.org/10.1088/0004-637X/807/2/154)
- Bovill, M. S., & Ricotti, M. 2009, *ApJ*, 693, 1859, doi: [10.1088/0004-637X/693/2/1859](https://doi.org/10.1088/0004-637X/693/2/1859)
- Boylan-Kolchin, M., & Weisz, D. R. 2021, *MNRAS*, 505, 2764, doi: [10.1093/mnras/stab1521](https://doi.org/10.1093/mnras/stab1521)
- Boylan-Kolchin, M., Weisz, D. R., Bullock, J. S., & Cooper, M. C. 2016, *MNRAS*, 462, L51, doi: [10.1093/mnrasl/slwl121](https://doi.org/10.1093/mnrasl/slwl121)
- Breddels, M. A., & Veljanoski, J. 2018a., *Astrophysics Source Code Library*, record ascl:1810.004 <http://ascl.net/1810.004>
- Breddels, M. A., & Veljanoski, J. 2018b, *A&A*, 618, A13, doi: [10.1051/0004-6361/201732493](https://doi.org/10.1051/0004-6361/201732493)
- Brown, T. M., Tumlinson, J., Geha, M., et al. 2014, *ApJ*, 796, 91, doi: [10.1088/0004-637X/796/2/91](https://doi.org/10.1088/0004-637X/796/2/91)
- Buck, T., Macciò, A. V., Dutton, A. A., Obreja, A., & Frings, J. 2019, *MNRAS*, 483, 1314, doi: [10.1093/mnras/sty2913](https://doi.org/10.1093/mnras/sty2913)
- Bullock, J. S., Kravtsov, A. V., & Weinberg, D. H. 2000, *ApJ*, 539, 517, doi: [10.1086/309279](https://doi.org/10.1086/309279)
- Busha, M. T., Alvarez, M. A., Wechsler, R. H., Abel, T., & Strigari, L. E. 2010, *ApJ*, 710, 408, doi: [10.1088/0004-637X/710/1/408](https://doi.org/10.1088/0004-637X/710/1/408)
- Carlin, J. L., Sand, D. J., Muñoz, R. R., et al. 2017, *AJ*, 154, 267, doi: [10.3847/1538-3881/aa94d0](https://doi.org/10.3847/1538-3881/aa94d0)
- Chambers, K. C., Magnier, E. A., Metcalfe, N., et al. 2016, *arXiv e-prints*, arXiv:1612.05560, doi: [10.48550/arXiv.1612.05560](https://doi.org/10.48550/arXiv.1612.05560)
- Cignoni, M., Sabbi, E., van der Marel, R. P., et al. 2015, *ApJ*, 811, 76, doi: [10.1088/0004-637X/811/2/76](https://doi.org/10.1088/0004-637X/811/2/76)
- Dalcanton, J. J., Fouesneau, M., Hogg, D. W., et al. 2015, *ApJ*, 814, 3, doi: [10.1088/0004-637X/814/1/3](https://doi.org/10.1088/0004-637X/814/1/3)
- D'Aloisio, A., McQuinn, M., & Trac, H. 2015, *ApJL*, 813, L38, doi: [10.1088/2041-8205/813/2/L38](https://doi.org/10.1088/2041-8205/813/2/L38)
- Dawoodbhoy, T., Shapiro, P. R., Ocvirk, P., et al. 2018, *MNRAS*, 480, 1740, doi: [10.1093/mnras/sty1945](https://doi.org/10.1093/mnras/sty1945)
- de Jong, J. T. A., Rix, H. W., Martin, N. F., et al. 2008, *AJ*, 135, 1361, doi: [10.1088/0004-6256/135/4/1361](https://doi.org/10.1088/0004-6256/135/4/1361)
- de Jong, J. T. A., Yanny, B., Rix, H.-W., et al. 2010, *ApJ*, 714, 663, doi: [10.1088/0004-637X/714/1/663](https://doi.org/10.1088/0004-637X/714/1/663)
- Delchambre, L., Bailer-Jones, C. A. L., Bellas-Velidis, I., et al. 2023, *A&A*, 674, A31, doi: [10.1051/0004-6361/202243423](https://doi.org/10.1051/0004-6361/202243423)
- Dolphin, A. 2016., *Astrophysics Source Code Library*, record ascl:1608.013 <http://ascl.net/1608.013>
- Dolphin, A. E. 2000, *PASP*, 112, 1383, doi: [10.1086/316630](https://doi.org/10.1086/316630)
- Dolphin, A. E. 2002, *MNRAS*, 332, 91, doi: [10.1046/j.1365-8711.2002.05271.x](https://doi.org/10.1046/j.1365-8711.2002.05271.x)
- Dolphin, A. E. 2012, *ApJ*, 751, 60, doi: [10.1088/0004-637X/751/1/60](https://doi.org/10.1088/0004-637X/751/1/60)
- Dolphin, A. E. 2013, *ApJ*, 775, 76, doi: [10.1088/0004-637X/775/1/76](https://doi.org/10.1088/0004-637X/775/1/76)
- Dotter, A. 2016, *ApJS*, 222, 8, doi: [10.3847/0067-0049/222/1/8](https://doi.org/10.3847/0067-0049/222/1/8)
- Drlica-Wagner, A., Bechtol, K., Rykoff, E. S., et al. 2015, *ApJ*, 813, 109, doi: [10.1088/0004-637X/813/2/109](https://doi.org/10.1088/0004-637X/813/2/109)
- Duane, S., Kennedy, A. D., Pendleton, B. J., & Roweth, D. 1987, *Physics Letters B*, 195, 216, doi: [10.1016/0370-2693\(87\)91197-X](https://doi.org/10.1016/0370-2693(87)91197-X)
- Efstathiou, G. 1992, *MNRAS*, 256, 43P, doi: [10.1093/mnras/256.1.43P](https://doi.org/10.1093/mnras/256.1.43P)
- Endsley, R., Stark, D. P., Charlot, S., et al. 2021, *MNRAS*, 502, 6044, doi: [10.1093/mnras/stab432](https://doi.org/10.1093/mnras/stab432)
- Engler, C., Pillepich, A., Pasquali, A., et al. 2021, *MNRAS*, 507, 4211, doi: [10.1093/mnras/stab2437](https://doi.org/10.1093/mnras/stab2437)
- Escala, I., Wetzell, A., Kirby, E. N., et al. 2018, *MNRAS*, 474, 2194, doi: [10.1093/mnras/stx2858](https://doi.org/10.1093/mnras/stx2858)
- Ferraro, S., & Smith, K. M. 2018, *PhRvD*, 98, 123519, doi: [10.1103/PhysRevD.98.123519](https://doi.org/10.1103/PhysRevD.98.123519)
- Fillingham, S. P., Cooper, M. C., Kelley, T., et al. 2019, *arXiv e-prints*, arXiv:1906.04180, doi: [10.48550/arXiv.1906.04180](https://doi.org/10.48550/arXiv.1906.04180)
- Flewelling, H. A., Magnier, E. A., Chambers, K. C., et al. 2020, *ApJS*, 251, 7, doi: [10.3847/1538-4365/abb82d](https://doi.org/10.3847/1538-4365/abb82d)
- Font, A. S., McCarthy, I. G., & Belokurov, V. 2021, *MNRAS*, 505, 783, doi: [10.1093/mnras/stab1332](https://doi.org/10.1093/mnras/stab1332)
- Fritz, T. K., Battaglia, G., Pawlowski, M. S., et al. 2018, *A&A*, 619, A103, doi: [10.1051/0004-6361/201833343](https://doi.org/10.1051/0004-6361/201833343)
- Fruchter, A. S., & Hook, R. N. 2002, *PASP*, 114, 144, doi: [10.1086/338393](https://doi.org/10.1086/338393)
- Fu, S. W., Weisz, D. R., Starkeburg, E., et al. 2023, *ApJ*, 958, 167, doi: [10.3847/1538-4357/ad0030](https://doi.org/10.3847/1538-4357/ad0030)
- Furlanetto, S. R., Oh, S. P., & Briggs, F. H. 2006, *PhR*, 433, 181, doi: [10.1016/j.physrep.2006.08.002](https://doi.org/10.1016/j.physrep.2006.08.002)
- Furlanetto, S. R., Zaldarriaga, M., & Hernquist, L. 2004, *ApJ*, 613, 1, doi: [10.1086/423025](https://doi.org/10.1086/423025)
- Gallart, C., & LCID Team. 2007, in *IAU Symposium*, Vol. 241, *Stellar Populations as Building Blocks of Galaxies*, ed. A. Vazdekis & R. Peletier, 290–294, doi: [10.1017/S1743921307008186](https://doi.org/10.1017/S1743921307008186)
- Gallart, C., Monelli, M., Ruiz-Lara, T., et al. 2021, *ApJ*, 909, 192, doi: [10.3847/1538-4357/abddbe](https://doi.org/10.3847/1538-4357/abddbe)
- Garling, C. T., Kallivayalil, N., McQuinn, K. B. W., et al. 2024, *arXiv e-prints*, arXiv:2407.19534, doi: [10.48550/arXiv.2407.19534](https://doi.org/10.48550/arXiv.2407.19534)
- Garrison-Kimmel, S., Wetzell, A., Hopkins, P. F., et al. 2019, *MNRAS*, 489, 4574, doi: [10.1093/mnras/stz2507](https://doi.org/10.1093/mnras/stz2507)

- Gilmore, G., Norris, J. E., Monaco, L., et al. 2013, *ApJ*, 763, 61, doi: [10.1088/0004-637X/763/1/61](https://doi.org/10.1088/0004-637X/763/1/61)
- Ginsburg, A., Parikh, M., Woillez, J., et al. 2017, <http://ascl.net/1708.004>
- Ginsburg, A., Sipőcz, B. M., Brasseur, C. E., et al. 2019, *AJ*, 157, 98, doi: [10.3847/1538-3881/aafc33](https://doi.org/10.3847/1538-3881/aafc33)
- Ginsburg, A., Sipőcz, B., Parikh, M., et al. 2021., v0.4.5, Zenodo Zenodo, doi: [10.5281/zenodo.591669](https://doi.org/10.5281/zenodo.591669)
- Gonzaga, S., Hack, W., Fruchter, A., & Mack, J. 2012, *The DrizzlePac Handbook* (Baltimore: STScI)
- Green, G. M., Schlafly, E., Zucker, C., Speagle, J. S., & Finkbeiner, D. 2019, *ApJ*, 887, 93, doi: [10.3847/1538-4357/ab5362](https://doi.org/10.3847/1538-4357/ab5362)
- Hack, W. J., Dencheva, N., & Fruchter, A. S. 2013, in *Astronomical Society of the Pacific Conference Series*, Vol. 475, *Astronomical Data Analysis Software and Systems XXII*, ed. D. N. Friedel, 49
- Harris, C. R., Millman, K. J., van der Walt, S. J., et al. 2020, *Nature*, 585, 357, doi: [10.1038/s41586-020-2649-2](https://doi.org/10.1038/s41586-020-2649-2)
- Hidalgo, S. L., Pietrinferni, A., Cassisi, S., et al. 2018, *ApJ*, 856, 125, doi: [10.3847/1538-4357/aab158](https://doi.org/10.3847/1538-4357/aab158)
- Hoffmann, S. L., Mack, J., Avila, R., et al. 2021, in *American Astronomical Society Meeting Abstracts*, Vol. 53, *American Astronomical Society Meeting Abstracts*, 216.02
- Homma, D., Chiba, M., Okamoto, S., et al. 2016, *ApJ*, 832, 21, doi: [10.3847/0004-637X/832/1/21](https://doi.org/10.3847/0004-637X/832/1/21)
- Hunter, J. D. 2007, *Computing in Science and Engineering*, 9, 90, doi: [10.1109/MCSE.2007.55](https://doi.org/10.1109/MCSE.2007.55)
- Jeon, M., Besla, G., & Bromm, V. 2017, *ApJ*, 848, 85, doi: [10.3847/1538-4357/aa8c80](https://doi.org/10.3847/1538-4357/aa8c80)
- Ji, A. P., Simon, J. D., Frebel, A., Venn, K. A., & Hansen, T. T. 2019, *ApJ*, 870, 83, doi: [10.3847/1538-4357/aaf3bb](https://doi.org/10.3847/1538-4357/aaf3bb)
- Jin, X., Yang, J., Fan, X., et al. 2024, *ApJ*, 976, 93, doi: [10.3847/1538-4357/ad82de](https://doi.org/10.3847/1538-4357/ad82de)
- Kallivayalil, N., van der Marel, R. P., Besla, G., Anderson, J., & Alcock, C. 2013, *ApJ*, 764, 161, doi: [10.1088/0004-637X/764/2/161](https://doi.org/10.1088/0004-637X/764/2/161)
- Kallivayalil, N., Sales, L. V., Zivick, P., et al. 2018, *ApJ*, 867, 19, doi: [10.3847/1538-4357/aadfee](https://doi.org/10.3847/1538-4357/aadfee)
- Katz, H., Ramsay, M., Rosdahl, J., et al. 2020, *MNRAS*, 494, 2200, doi: [10.1093/mnras/staa639](https://doi.org/10.1093/mnras/staa639)
- Kim, J., Jeon, M., Choi, Y., et al. 2023, *ApJ*, 959, 31, doi: [10.3847/1538-4357/acfe08](https://doi.org/10.3847/1538-4357/acfe08)
- Kirby, E. N., Lanfranchi, G. A., Simon, J. D., Cohen, J. G., & Guhathakurta, P. 2011, *ApJ*, 727, 78, doi: [10.1088/0004-637X/727/2/78](https://doi.org/10.1088/0004-637X/727/2/78)
- Koposov, S. E., Walker, M. G., Belokurov, V., et al. 2018, *MNRAS*, 479, 5343, doi: [10.1093/mnras/sty1772](https://doi.org/10.1093/mnras/sty1772)
- Kroupa, P. 2001, *MNRAS*, 322, 231, doi: [10.1046/j.1365-8711.2001.04022.x](https://doi.org/10.1046/j.1365-8711.2001.04022.x)
- Laevens, B. P. M., Martin, N. F., Bernard, E. J., et al. 2015, *ApJ*, 813, 44, doi: [10.1088/0004-637X/813/1/44](https://doi.org/10.1088/0004-637X/813/1/44)
- Lallement, R., Vergely, J. L., Babusiaux, C., & Cox, N. L. J. 2022, *A&A*, 661, A147, doi: [10.1051/0004-6361/202142846](https://doi.org/10.1051/0004-6361/202142846)
- Lewis, A. R., Dolphin, A. E., Dalcanton, J. J., et al. 2015, *ApJ*, 805, 183, doi: [10.1088/0004-637X/805/2/183](https://doi.org/10.1088/0004-637X/805/2/183)
- Li, T. Y., Alvarez, M. A., Wechsler, R. H., & Abel, T. 2014, *ApJ*, 785, 134, doi: [10.1088/0004-637X/785/2/134](https://doi.org/10.1088/0004-637X/785/2/134)
- Longeard, N., Martin, N., Ibata, R. A., et al. 2021, *MNRAS*, 503, 2754, doi: [10.1093/mnras/stab604](https://doi.org/10.1093/mnras/stab604)
- Lunnan, R., Vogelsberger, M., Frebel, A., et al. 2012, *ApJ*, 746, 109, doi: [10.1088/0004-637X/746/1/109](https://doi.org/10.1088/0004-637X/746/1/109)
- Mack, J., Hack, W., Burger, M., et al. 2022., *Instrument Science Report ACS 2022-03*, 37 pages
- Martínez-Vázquez, C. E., Vivas, A. K., Gurevich, M., et al. 2019, *MNRAS*, 490, 2183, doi: [10.1093/mnras/stz2609](https://doi.org/10.1093/mnras/stz2609)
- McKinney, W. 2010, in *Proceedings of the 9th Python in Science Conference*, ed. S. van der Walt & Millman, Jarrod, *Proceedings of the Python in Science Conference (SciPy)*, 56–61, doi: [10.25080/Majora-92bf1922-00a](https://doi.org/10.25080/Majora-92bf1922-00a)
- McQuinn, K. B. W., Mao, Y.-Y., Buckley, M. R., et al. 2023, *ApJ*, 944, 14, doi: [10.3847/1538-4357/acaec9](https://doi.org/10.3847/1538-4357/acaec9)
- McQuinn, K. B. W., Mao, Y.-Y., Tollerud, E. J., et al. 2024, *ApJ*, 967, 161, doi: [10.3847/1538-4357/ad429b](https://doi.org/10.3847/1538-4357/ad429b)
- McQuinn, K. B. W., Skillman, E. D., Cannon, J. M., et al. 2010, *ApJ*, 721, 297, doi: [10.1088/0004-637X/721/1/297](https://doi.org/10.1088/0004-637X/721/1/297)
- McQuinn, K. B. W., Skillman, E. D., Dolphin, A., et al. 2015, *ApJ*, 812, 158, doi: [10.1088/0004-637X/812/2/158](https://doi.org/10.1088/0004-637X/812/2/158)
- McQuinn, M., Lidz, A., Zahn, O., et al. 2007, *MNRAS*, 377, 1043, doi: [10.1111/j.1365-2966.2007.11489.x](https://doi.org/10.1111/j.1365-2966.2007.11489.x)
- Monelli, M., Gallart, C., Hidalgo, S. L., et al. 2010, *ApJ*, 722, 1864, doi: [10.1088/0004-637X/722/2/1864](https://doi.org/10.1088/0004-637X/722/2/1864)
- Muñoz, J. A., Madau, P., Loeb, A., & Diemand, J. 2009, *MNRAS*, 400, 1593, doi: [10.1111/j.1365-2966.2009.15562.x](https://doi.org/10.1111/j.1365-2966.2009.15562.x)
- Muñoz, R. R., Côté, P., Santana, F. A., et al. 2018, *ApJ*, 860, 66, doi: [10.3847/1538-4357/aac16b](https://doi.org/10.3847/1538-4357/aac16b)
- Mutlu-Pakdil, B., Sand, D. J., Carlin, J. L., et al. 2018, *ApJ*, 863, 25, doi: [10.3847/1538-4357/aacd0e](https://doi.org/10.3847/1538-4357/aacd0e)
- Nagarajan, P., Weisz, D. R., & El-Badry, K. 2022, *ApJ*, 932, 19, doi: [10.3847/1538-4357/ac69e6](https://doi.org/10.3847/1538-4357/ac69e6)
- Nidever, D. L., Dey, A., Olsen, K., et al. 2018, *AJ*, 156, 131, doi: [10.3847/1538-3881/aad68f](https://doi.org/10.3847/1538-3881/aad68f)
- Nidever, D. L., Dey, A., Fasbender, K., et al. 2021, *AJ*, 161, 192, doi: [10.3847/1538-3881/abd6e1](https://doi.org/10.3847/1538-3881/abd6e1)
- Ochsenbein, F., Bauer, P., & Marcout, J. 2000, *A&AS*, 143, 23, doi: [10.1051/aas:2000169](https://doi.org/10.1051/aas:2000169)

- Ocvirk, P., Aubert, D., Sorce, J. G., et al. 2020, *MNRAS*, 496, 4087, doi: [10.1093/mnras/staa1266](https://doi.org/10.1093/mnras/staa1266)
- Okamoto, S., Arimoto, N., Yamada, Y., & Onodera, M. 2012, *ApJ*, 744, 96, doi: [10.1088/0004-637X/744/2/96](https://doi.org/10.1088/0004-637X/744/2/96)
- Pace, A. B. 2024, arXiv e-prints, arXiv:2411.07424, doi: [10.48550/arXiv.2411.07424](https://doi.org/10.48550/arXiv.2411.07424)
- Pace, A. B., Erkal, D., & Li, T. S. 2022, *ApJ*, 940, 136, doi: [10.3847/1538-4357/ac997b](https://doi.org/10.3847/1538-4357/ac997b)
- Patel, E., Kallivayalil, N., Garavito-Camargo, N., et al. 2020, *ApJ*, 893, 121, doi: [10.3847/1538-4357/ab7b75](https://doi.org/10.3847/1538-4357/ab7b75)
- Pentericci, L., Vanzella, E., Fontana, A., et al. 2014, *ApJ*, 793, 113, doi: [10.1088/0004-637X/793/2/113](https://doi.org/10.1088/0004-637X/793/2/113)
- Pietrinferni, A., Cassisi, S., Salaris, M., & Castelli, F. 2004, *ApJ*, 612, 168, doi: [10.1086/422498](https://doi.org/10.1086/422498)
- Pietrinferni, A., Hidalgo, S., Cassisi, S., et al. 2021, *ApJ*, 908, 102, doi: [10.3847/1538-4357/abd4d5](https://doi.org/10.3847/1538-4357/abd4d5)
- Planck Collaboration, Aghanim, N., Akrami, Y., et al. 2020, *A&A*, 641, A6, doi: [10.1051/0004-6361/201833910](https://doi.org/10.1051/0004-6361/201833910)
- Richstein, H., Patel, E., Kallivayalil, N., et al. 2022, *ApJ*, 933, 217, doi: [10.3847/1538-4357/ac7226](https://doi.org/10.3847/1538-4357/ac7226)
- Ricotti, M., & Gnedin, N. Y. 2005, *ApJ*, 629, 259, doi: [10.1086/431415](https://doi.org/10.1086/431415)
- Robertson, B. E., Ellis, R. S., Dunlop, J. S., McLure, R. J., & Stark, D. P. 2010, *Nature*, 468, 49, doi: [10.1038/nature09527](https://doi.org/10.1038/nature09527)
- Rodriguez Wimberly, M. K., Cooper, M. C., Fillingham, S. P., et al. 2019, *MNRAS*, 483, 4031, doi: [10.1093/mnras/sty3357](https://doi.org/10.1093/mnras/sty3357)
- Sacchi, E., Richstein, H., Kallivayalil, N., et al. 2021, *ApJL*, 920, L19, doi: [10.3847/2041-8213/ac2aa3](https://doi.org/10.3847/2041-8213/ac2aa3)
- Sales, L. V., Navarro, J. F., Kallivayalil, N., & Frenk, C. S. 2017, *MNRAS*, 465, 1879, doi: [10.1093/mnras/stw2816](https://doi.org/10.1093/mnras/stw2816)
- Salvadori, S., & Ferrara, A. 2009, *MNRAS*, 395, L6, doi: [10.1111/j.1745-3933.2009.00627.x](https://doi.org/10.1111/j.1745-3933.2009.00627.x)
- Santistevan, I. B., Wetzell, A., Tollerud, E., Sanderson, R. E., & Samuel, J. 2023, *MNRAS*, 518, 1427, doi: [10.1093/mnras/stac3100](https://doi.org/10.1093/mnras/stac3100)
- Savino, A., Weisz, D. R., Skillman, E. D., et al. 2023, *ApJ*, 956, 86, doi: [10.3847/1538-4357/acf46f](https://doi.org/10.3847/1538-4357/acf46f)
- Savino, A., Weisz, D. R., Dolphin, A. E., et al. 2025, *ApJ*, 979, 205, doi: [10.3847/1538-4357/ada24f](https://doi.org/10.3847/1538-4357/ada24f)
- Sawala, T., Frenk, C. S., Fattahi, A., et al. 2016, *MNRAS*, 456, 85, doi: [10.1093/mnras/stv2597](https://doi.org/10.1093/mnras/stv2597)
- Schlafly, E. F., & Finkbeiner, D. P. 2011, *ApJ*, 737, 103, doi: [10.1088/0004-637X/737/2/103](https://doi.org/10.1088/0004-637X/737/2/103)
- Schlegel, D. J., Finkbeiner, D. P., & Davis, M. 1998, *ApJ*, 500, 525, doi: [10.1086/305772](https://doi.org/10.1086/305772)
- Simon, J. D. 2019, *ARA&A*, 57, 375, doi: [10.1146/annurev-astro-091918-104453](https://doi.org/10.1146/annurev-astro-091918-104453)
- Simon, J. D., Frebel, A., McWilliam, A., Kirby, E. N., & Thompson, I. B. 2010, *ApJ*, 716, 446, doi: [10.1088/0004-637X/716/1/446](https://doi.org/10.1088/0004-637X/716/1/446)
- Simon, J. D., Li, T. S., Erkal, D., et al. 2020, *ApJ*, 892, 137, doi: [10.3847/1538-4357/ab7ccb](https://doi.org/10.3847/1538-4357/ab7ccb)
- Simon, J. D., Brown, T. M., Drlica-Wagner, A., et al. 2021, *ApJ*, 908, 18, doi: [10.3847/1538-4357/abd31b](https://doi.org/10.3847/1538-4357/abd31b)
- Simon, J. D., Brown, T. M., Mutlu-Pakdil, B., et al. 2023, *ApJ*, 944, 43, doi: [10.3847/1538-4357/aca9d1](https://doi.org/10.3847/1538-4357/aca9d1)
- Simon, J. D., Li, T. S., Ji, A. P., et al. 2024, *ApJ*, 976, 256, doi: [10.3847/1538-4357/ad85dd](https://doi.org/10.3847/1538-4357/ad85dd)
- Simpson, C. M., Bryan, G. L., Johnston, K. V., et al. 2013, *MNRAS*, 432, 1989, doi: [10.1093/mnras/stt474](https://doi.org/10.1093/mnras/stt474)
- Simpson, C. M., Grand, R. J. J., Gómez, F. A., et al. 2018, *MNRAS*, 478, 548, doi: [10.1093/mnras/sty774](https://doi.org/10.1093/mnras/sty774)
- Skillman, E. D., Tolstoy, E., Cole, A. A., et al. 2003, *ApJ*, 596, 253, doi: [10.1086/377635](https://doi.org/10.1086/377635)
- Skillman, E. D., Monelli, M., Weisz, D. R., et al. 2017, *ApJ*, 837, 102, doi: [10.3847/1538-4357/aa60c5](https://doi.org/10.3847/1538-4357/aa60c5)
- Smith, K. M., & Ferraro, S. 2017, *PhRvL*, 119, 021301, doi: [10.1103/PhysRevLett.119.021301](https://doi.org/10.1103/PhysRevLett.119.021301)
- Sobacchi, E., & Mesinger, A. 2013, *MNRAS*, 432, L51, doi: [10.1093/mnras/slt035](https://doi.org/10.1093/mnras/slt035)
- Somerville, R. S. 2002, *ApJL*, 572, L23, doi: [10.1086/341444](https://doi.org/10.1086/341444)
- Sorce, J. G., Ocvirk, P., Aubert, D., et al. 2022, *MNRAS*, 515, 2970, doi: [10.1093/mnras/stac2007](https://doi.org/10.1093/mnras/stac2007)
- STSCI Development Team. 2012., Astrophysics Source Code Library, record ascl:1212.011 <http://ascl.net/1212.011>
- The Matplotlib Development Team. 2023., v3.8.1, Zenodo Zenodo, doi: [10.5281/zenodo.592536](https://doi.org/10.5281/zenodo.592536)
- The pandas development Team. 2023., v2.1.2, Zenodo Zenodo, doi: [10.5281/zenodo.3509134](https://doi.org/10.5281/zenodo.3509134)
- Tumlinson, J. 2010, *ApJ*, 708, 1398, doi: [10.1088/0004-637X/708/2/1398](https://doi.org/10.1088/0004-637X/708/2/1398)
- van der Walt, S., Colbert, S. C., & Varoquaux, G. 2011, *Computing in Science and Engineering*, 13, 22, doi: [10.1109/MCSE.2011.37](https://doi.org/10.1109/MCSE.2011.37)
- VandenBerg, D. A., Bergbusch, P. A., & Dowler, P. D. 2014a., Astrophysics Source Code Library, record ascl:1404.010
- VandenBerg, D. A., Bergbusch, P. A., Ferguson, J. W., & Edvardsson, B. 2014b, *ApJ*, 794, 72, doi: [10.1088/0004-637X/794/1/72](https://doi.org/10.1088/0004-637X/794/1/72)
- Vargas, L. C., Geha, M., Kirby, E. N., & Simon, J. D. 2013, *ApJ*, 767, 134, doi: [10.1088/0004-637X/767/2/134](https://doi.org/10.1088/0004-637X/767/2/134)
- Virtanen, P., Gommers, R., Oliphant, T. E., et al. 2020, *Nature Methods*, 17, 261, doi: [10.1038/s41592-019-0686-2](https://doi.org/10.1038/s41592-019-0686-2)
- Vivas, A. K., Martínez-Vázquez, C., & Walker, A. R. 2020, *ApJS*, 247, 35, doi: [10.3847/1538-4365/ab67c0](https://doi.org/10.3847/1538-4365/ab67c0)

- Waskom, M. 2021, *The Journal of Open Source Software*, 6, 3021, doi: [10.21105/joss.03021](https://doi.org/10.21105/joss.03021)
- Waskom, M., Botvinnik, O., Gelbart, M., et al. 2020,, *Astrophysics Source Code Library*, record ascl:2012.015 <http://ascl.net/2012.015>
- Waskom, M., Gelbart, M., Botvinnik, O., et al. 2023,, v0.13.0, *Zenodo* Zenodo, doi: [10.5281/zenodo.592845](https://doi.org/10.5281/zenodo.592845)
- Webster, D., Bland-Hawthorn, J., & Sutherland, R. 2015, *ApJL*, 799, L21, doi: [10.1088/2041-8205/799/2/L21](https://doi.org/10.1088/2041-8205/799/2/L21)
- Weisz, D. R., Dolphin, A. E., Skillman, E. D., et al. 2014a, *ApJ*, 789, 148, doi: [10.1088/0004-637X/789/2/148](https://doi.org/10.1088/0004-637X/789/2/148)
- Weisz, D. R., Dolphin, A. E., Skillman, E. D., et al. 2014b, *ApJ*, 789, 147, doi: [10.1088/0004-637X/789/2/147](https://doi.org/10.1088/0004-637X/789/2/147)
- Weisz, D. R., Dolphin, A. E., Skillman, E. D., et al. 2015, *ApJ*, 804, 136, doi: [10.1088/0004-637X/804/2/136](https://doi.org/10.1088/0004-637X/804/2/136)
- Weisz, D. R., Savino, A., & Dolphin, A. E. 2023, *ApJ*, 948, 50, doi: [10.3847/1538-4357/acc328](https://doi.org/10.3847/1538-4357/acc328)
- Weisz, D. R., Dolphin, A. E., Dalcanton, J. J., et al. 2011a, *ApJ*, 743, 8, doi: [10.1088/0004-637X/743/1/8](https://doi.org/10.1088/0004-637X/743/1/8)
- Weisz, D. R., Dalcanton, J. J., Williams, B. F., et al. 2011b, *ApJ*, 739, 5, doi: [10.1088/0004-637X/739/1/5](https://doi.org/10.1088/0004-637X/739/1/5)
- Weisz, D. R., Zucker, D. B., Dolphin, A. E., et al. 2012, *ApJ*, 748, 88, doi: [10.1088/0004-637X/748/2/88](https://doi.org/10.1088/0004-637X/748/2/88)
- Wetzell, A. R., Deason, A. J., & Garrison-Kimmel, S. 2015, *ApJ*, 807, 49, doi: [10.1088/0004-637X/807/1/49](https://doi.org/10.1088/0004-637X/807/1/49)
- Wetzell, A. R., Hopkins, P. F., Kim, J.-h., et al. 2016, *ApJL*, 827, L23, doi: [10.3847/2041-8205/827/2/L23](https://doi.org/10.3847/2041-8205/827/2/L23)
- Wheeler, C., Oñorbe, J., Bullock, J. S., et al. 2015, *MNRAS*, 453, 1305, doi: [10.1093/mnras/stv1691](https://doi.org/10.1093/mnras/stv1691)
- Williams, B. F., Dalcanton, J. J., Seth, A. C., et al. 2009, *AJ*, 137, 419, doi: [10.1088/0004-6256/137/1/419](https://doi.org/10.1088/0004-6256/137/1/419)
- Williams, B. F., Lang, D., Dalcanton, J. J., et al. 2014, *ApJS*, 215, 9, doi: [10.1088/0067-0049/215/1/9](https://doi.org/10.1088/0067-0049/215/1/9)
- Williams, B. F., Durbin, M. J., Dalcanton, J. J., et al. 2021, *ApJS*, 253, 53, doi: [10.3847/1538-4365/abdf4e](https://doi.org/10.3847/1538-4365/abdf4e)
- Williams, B. F., Durbin, M., Lang, D., et al. 2023, *ApJS*, 268, 48, doi: [10.3847/1538-4365/acea61](https://doi.org/10.3847/1538-4365/acea61)
- Zaremba, D., Venn, K., Hayes, C. R., et al. 2025, arXiv e-prints, arXiv:2503.05927, doi: [10.48550/arXiv.2503.05927](https://doi.org/10.48550/arXiv.2503.05927)
- Zhao, Y., Smith, A., Kannan, R., et al. 2025, arXiv e-prints, arXiv:2507.16245, doi: [10.48550/arXiv.2507.16245](https://doi.org/10.48550/arXiv.2507.16245)
- Zhu, H., Avestruz, C., & Gnedin, N. Y. 2019, *ApJ*, 882, 152, doi: [10.3847/1538-4357/ab3794](https://doi.org/10.3847/1538-4357/ab3794)
- Zier, O., Kannan, R., Smith, A., et al. 2025, arXiv e-prints, arXiv:2503.02927, doi: [10.48550/arXiv.2503.02927](https://doi.org/10.48550/arXiv.2503.02927)